A&A, 693, A212 (2025)
https://doi.org/10.1051/0004-6361/202449416

Astronomy & Astrophysics

The eROSITA Final Equatorial Depth Survey (eFEDS)

The hard X-ray selected sample

K. Nandra[1,⋆], S. G. H. Waddell[1], T. Liu[1], J. Buchner[1], T. Dwelly[1], M. Salvato[1], Y. Shen[2], Q. Wu[2], R. Arcodia[1], Th. Boller[1], H. Brunner[1], M. Brusa[3,4], W. Collmar[1], J. Comparat[1], A. Georgakakis[5], M. Grau[1], S. Hämmerich[6], H. Ibarra-Medel[8], Z. Igo[1], M. Krumpe[7], G. Lamer[7], A. Merloni[1], B. Musiimenta[3,4], J. Wolf[1], R. J. Assef[9], F. E. Bauer[10,11,12,13], W. N. Brandt[14,15,16], and H.-W. Rix[17]

[1] Max Planck Institute for Extraterrestrial Physics (MPE), Giessenbachstrasse 1, 85748 Garching bei München, Germany
[2] Department of Astronomy, University of Illinois at Urbana-Champaign, Urbana, IL 61801, USA
[3] Dipartimento di Fisica e Astronomia 'Augusto Righi', Alma Mater Studiorum Università di Bologna, via Gobetti 93/2, 40129 Bologna, Italy
[4] INAF-Osservatorio di Astrofisica e Scienza dello Spazio di Bologna, via Gobetti 93/3, 40129 Bologna, Italy
[5] Institute for Astronomy and Astrophysics, National Observatory of Athens, V. Paulou and I. Metaxa, 11532, Greece
[6] Dr. Karl Remeis-Sternwarte and Erlangen Centre for Astroparticle Physics, Friedrich-Alexander Universität Erlangen-Nürnberg, Sternwartstraße 7, 96049 Bamberg, Germany
[7] Leibniz-Institut für Astrophysik Potsdam (AIP), An der Sternwarte 16, 14482 Potsdam, Germany
[8] Instituto de Astronomía y Ciencias Planetarias, Universidad de Atacama, Copayapu 485, Copiapó, Chile
[9] Instituto de Estudios Astrofísicos, Facultad de Ingeniería y Ciencias, Universidad Diego Portales, Av. Ejército Libertador 441, Santiago, Chile
[10] Instituto de Astrofísica, Facultad de Física, Pontificia Universidad Católica de Chile, Campus San Joaquín, Av. Vicuña Mackenna 4860, Macul Santiago 7820436, Chile
[11] Centro de Astroingeniería, Facultad de Física, Pontificia Universidad Católica de Chile, Campus San Joaquín, Av. Vicuña Mackenna 4860, Macul Santiago 7820436, Chile
[12] Millennium Institute of Astrophysics, Nuncio Monseñor Sótero Sanz 100, Of 104, Providencia, Santiago, Chile
[13] Space Science Institute, 4750 Walnut Street, Suite 205, Boulder, CO 80301, USA
[14] Department of Astronomy & Astrophysics, 525 Davey Lab, The Pennsylvania State University, University Park, PA 16802, USA
[15] Institute for Gravitation and the Cosmos, The Pennsylvania State University, University Park, PA 16802, USA
[16] Department of Physics, 104 Davey Laboratory, The Pennsylvania State University, University Park, PA 16802, USA
[17] Max-Planck-Institut für Astronomie, Königstuhl 17, 69117 Heidelberg, Germany

Received 30 January 2024 / Accepted 12 July 2024

ABSTRACT

Context. During its calibration and performance verification phase, the eROSITA instrument aboard the Spectrum-RG satellite performed a uniform wide-area X-ray survey of approximately 140 deg^2, known as the eROSITA Final Equatorial Depth Survey (eFEDS).
Aims. The primary aim of eFEDS is to demonstrate the scientific performance to be expected at the end of the eight–pass eROSITA all–sky survey. This survey will provide the first focussed image of the whole sky in the hard X-ray (>2 keV) bandpass. The expected source population in this energy range is thus of great interest, particularly for AGN studies.
Methods. We used a 2.3–5 keV selection to construct a sample of 246 point-like hard X-ray sources for further study and characterisation. These sources are classified as either extragalactic (~90%) or Galactic (~10%), with the former consisting overwhelmingly of AGN and the latter active stars. We concentrated our further analysis on the extragalactic AGN sample, describing their X-ray and multi-wavelength properties and comparing them to the eFEDS main AGN sample selected in the softer 0.2–2.3 keV band.
Results. The eROSITA hard band selects a subsample of sources that is a factor of more than ten brighter than the eFEDS main sample. The AGN within the hard population reach up to $z = 3.2$ but on the whole, they are relatively nearby, with median $z = 0.34$ compared to z=0.94 for the main sample. The hard survey probes typical luminosities in the range $\log L_X = 43$–46. The X-ray spectral analysis shows significant intrinsic absorption (with $\log N_H > 21$) in ~20% of the sources, with a hard X-ray power law continuum with mean $< \Gamma >= 1.83 \pm 0.04$, which is typical of AGN, but slightly harder than the soft-selected eROSITA sample. Around 10% of the hard sample show a significant 'soft excess' component. The sampled black hole mass distribution in the eFEDS broad-line AGN population is consistent with that of the deeper COSMOS survey that probes a higher redshift population. On the other hand, the Eddington ratios appear systematically lower, which is consistent with the idea that the decline in SMBH activity since $z \sim 1$ is due to a reduction in the typical accretion rate, rather than a shift towards activity in lower-mass black holes.
Conclusions. The eFEDS hard sample provides a preview of what can be expected from the eRASS final survey in terms of data quality. This pilot survey indicates the power of eROSITA to shed new light on the demographics and evolution of AGN, and the potential for discovery of new and rare populations.

Key words. catalogs – surveys – galaxies: active

[⋆] Corresponding author; `knandra@mpe.mpg.de`

1. Introduction

The eROSITA instrument (Predehl et al. 2021) aboard the Spectrum-Röntgen-Gamma (SRG) satellite (Sunyaev et al. 2021) consists of seven Wolter-1 type telescopes focussing X-rays onto seven focal plane X-ray cameras. It is designed to survey the sky in the X-ray band, with the driving science being to constrain the cosmological parameters via the evolution of clusters of galaxies (Merloni et al. 2012). A key aim is to detect all clusters in the Universe more massive than about $3 \times 10^{14} M_{\odot}$. This requires all-sky coverage with high surface-brightness sensitivity, combined with angular resolution sufficient to resolve clusters from the much larger population of X-ray point sources in the sky, dominated by active galactic nuclei (AGN) and coronally active stars. To do this efficiently requires an imaging telescope with large field of view and effective area in the soft X-ray band.

While the primary driving science of eROSITA is cluster cosmology, the high sensitivity of the instrument and mission profile of SRG enable a vast array of additional science (Merloni et al. 2012). Unlike its predecessor ROSAT (Truemper 1982), the eROSITA telescope system features significant effective area in the harder X-ray band above 2 keV. Together with its sister instrument Mikhail Pavlinsky ART-XC (Pavlinsky et al. 2021), which covers an even harder X-ray band (4–30 keV), it is the first focussing telescope to have performed an all-sky survey at energies above 2 keV. Therefore, eROSITA opens up a new parameter space for large-area hard X-ray surveys.

These SRG surveys build on a considerable body of work in this energy range that have covered various regions of area-depth parameter space. One early example is the HEAO-1 A2 survey, which covered the whole sky. Despite its high flux limit, this survey has nonetheless been very influential as it established a reference set of X-ray bright extragalactic objects (Piccinotti et al. 1982) that have been the subject of increasingly intense study by subsequent X-ray missions. Numerically, the extragalactic hard X-ray population found by HEAO-1 was dominated by AGN hosting accreting supermassive black holes, with the next most numerous class being massive clusters of galaxies.

While soft X-ray surveys, such as those performed by ROSAT and now eROSITA, are arguably more efficient for the selection of galaxy clusters, harder X-ray surveys are of particular interest for AGN studies. One reason for this is that hard X-ray emission can be used to uncover heavily obscured AGN and measure their level of obscuration (e.g. Awaki et al. 1991; Turner et al. 1997), as well as their contribution to the X-ray background (e.g. Comastri et al. 1995; Gilli et al. 2007; Ueda et al. 2014). These factors have motivated numerous surveys with X-ray imaging telescopes that are sensitive above 2 keV, for example with *ASCA* (Ueda et al. 1999), *BeppoSAX* (Fiore et al. 2001), *Chandra* (e.g. Nandra et al. 2015; Civano et al. 2016; Luo et al. 2017) and *XMM-Newton* (e.g. Fiore et al. 2003; Hasinger et al. 2007; Ranalli et al. 2013; Pierre et al. 2016). Even harder bandpasses with greater sensitivity to the most heavily obscured AGN have also been covered by *Swift* (Oh et al. 2018) and *NuSTAR* (Alexander et al. 2013). These and other similar surveys have formed the backbone of the AGN demographic and evolutionary studies over the past two decades (e.g. Ueda et al. 2003; La Franca et al. 2005; Aird et al. 2015; Buchner et al. 2015). Despite the great depth of surveys in particular with *Chandra* and *XMM-Newton*, they can only cover limited areas. For example, the largest area surveys with each facility XBootes (Murray et al. 2005; Kenter et al. 2005) and XMM-XXL (Pierre et al. 2016) reach flux limits of around 2×10^{-14} erg cm^{-2} s^{-1} in the 2–10 keV band but cover only nine and (two) 25 deg^2 contiguous regions respectively. A significant region of parameter space exists in between these *Chandra* or *XMM-Newton* surveys and those with HEAO-1 A2 (Piccinotti et al. 1982) or the similar depth RXTE All-Sky Survey (Revnivtsev et al. 2004), the last two cover the whole sky but at a flux limit around three orders of magnitude brighter. This gap in depth-area coverage can neatly be filled by a wide-field imaging X-ray telescope such as eROSITA.

As a precursor to the eROSITA all-sky survey (eRASS), eROSITA performed a field scan of an equatorial region of approximately 140 deg^2 during its calibration and performance verification phase. Aside from all-sky surveys such as ROSAT and the eRASS itself, this survey, known as the eROSITA Final Equatorial Depth Survey (eFEDS) currently represents the largest contiguous dedicated X-ray imaging survey performed thus far, despite taking only approximately five days. Occupying a new part of area-depth parameter space for contiguous surveys (Brunner et al. 2022), and with excellent supporting data in numerous other wavebands, eFEDS is capable of yielding new insights, particularly into the properties and evolution of clusters and AGN. It also provides a verification and foretaste of what can ultimately be expected from the full four-year exposure of the entire sky (eRASS:8).

In this paper, we present an analysis of the X-ray and optical properties of the hard X-ray (2.3–5 keV) point sources detected in eFEDS. In Sect. 2 we briefly describe the sources of the data and the methodology from which the catalogue products were derived. Sect. 3 presents the basic properties of the sample. In Sect. 4 we focus on the subsample of extragalactic sources, predominantly AGN. A discussion and outlook for the eventual eight-pass, four-year eRASS:8 all-sky survey is presented in Sect. 5.

Throughout this paper, we adopt a flat Λ cold dark matter cosmology with $\Omega_{\Lambda} = 0.7$, $\Omega_m = 0.3$, and $H_0 = 70$ km s^{-1} Mpc^{-1}.

2. Data and methods

2.1. The eROSITA final equatorial depth survey

A full description of the eFEDS X-ray survey is presented in Brunner et al. (2022), which also contains the X-ray catalogue used to construct the sample presented in this paper. The eFEDS field covers approximately 140 deg^2 in an equatorial field chosen to have excellent multi-wavelength supporting data. Of particular note for the current study are (i) the high quality optical imaging and photometry provided by the HSC Wide Area Survey (Aihara et al. 2018); (ii) multi-band photometry from the DESI Legacy Imaging survey (Dey et al. 2019) data release eight (LS8), which also incorporates mid-infrared data from the Wide-Field Infrared Spectroscopic Explorer (WISE; Wright et al. 2010) and (iii) extensive optical spectroscopic coverage mainly from the fourth and fifth incarnations of the Sloan Digital Sky Survey (SDSS; Blanton et al. 2017; Kollmeier et al. 2017, Kollmeier et al., in prep). A more complete description of the multi-wavelength data in this field can be found in Salvato et al. (2022).

The X-ray data were acquired in a field-scanning mode providing an unusually uniform exposure over the field compared to the ‘point and stare’ observing strategy commonly used for X-ray surveys. The nominal exposure at a given position is typically 2.2ks, making the eFEDS survey representative of, but slightly deeper than, the expectation for the typical equatorial sky position in the full 8-pass eRASS:8.

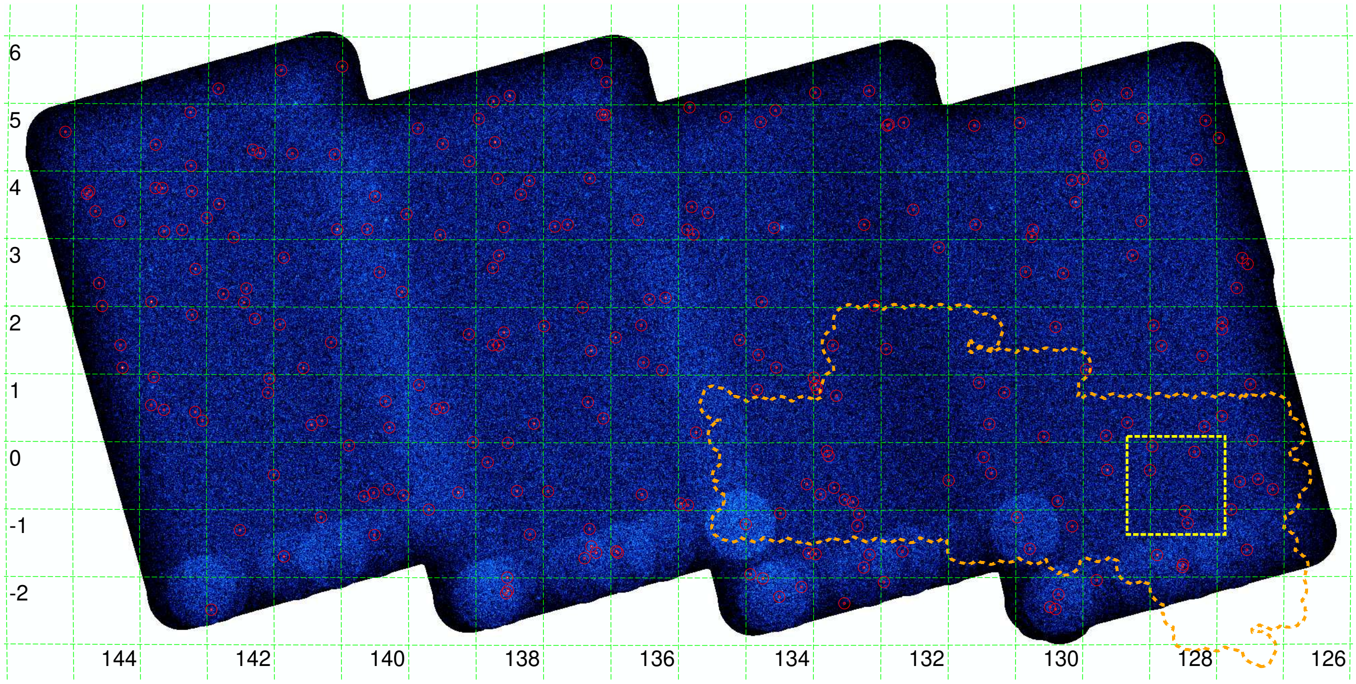

Fig. 1. eFEDS imagine in the 2.3–5 keV band, smoothed by a Gaussian kernel of $\sigma = 16''$, with each point source overlaid as a red annulus with radii of 60″ and 300″. Representations of the regions of the XMM-XXL-north (orange) and the COSMOS (yellow) fields, which do not overlap with eFEDS, are placed at the lower right corner for size comparison.

The X-ray data processing and reduction was performed using the eROSITA Science Analysis Software system (eSASS) using the eROSITA early data release (EDR) version (eSASSusers_201009). The eSASS processing chain is described in full in Brunner et al. (2022). Source detection involves the generation of an initial seed source catalogue using a sliding box detection algorithm, and subsequent point-spread-function (PSF) fitting to determine source counts and significances using a likelihood ratio approach. An advantage to this method is that the detection can be performed using event files or images in multiple energy bands simultaneously. In practice, the eFEDS main sample is assembled using a soft X-ray selection in the 0.2–2.3 keV band, where the instrument is most sensitive. This main eFEDS source catalogue contains a total of 27 910 sources above a detection likelihood threshold `DET_LIKE`> 6 in the detection band, where `DET_LIKE`$= -\ln P$ where P is the chance probability of the source being a background fluctuation based on a point-spread-function-fitting detection algorithm (see Brunner et al. 2022). The detection algorithm allows for the sources to be extended, also providing a likelihood estimation for this, the quantity `EXT_LIKE`. Sources with `EXT_LIKE`>= 6 are considered candidate galaxy clusters whose properties are presented and analysed in detail by Liu et al. (2022a). Sources with `EXT_LIKE`< 6 are considered point-like and have their `EXT_LIKE` fixed to zero in the catalogue of Brunner et al. (2022). The point sources can have a variety of classifications, and are characterised by a dedicated algorithm (see below and Salvato et al. 2022).

2.2. The eFEDS hard X-ray catalogue

To supplement the main, soft X-ray source catalogue, Brunner et al. (2022) also present a hard X-ray-selected catalogue. This is constructed using a source-detection run performed simultaneously in three energy bands: 0.2–0.6, 0.6–2.3 and 2.3–5 keV (see Brunner et al. 2022, for details), which results in a likelihood in each of the individual bands, as well as a combined likelihood for all three bands. To construct the catalogue presented here, a threshold of the three-band summary likelihood `DET_LIKE_0`> 5 was adopted. We then selected sources with a detection likelihood in the hardest of those three bands (2.3–5 keV) of `DET_LIKE_3`> 10. The former threshold is sufficiently loose that it has no impact on the latter, in other words, the `DET_LIKE_0`> 5 threshold does not remove any potential source with `DET_LIKE_3`> 10. There are eight extended sources with `DET_LIKE_3`> 10 and `EXT_LIKE`>= 6 that are candidate galaxy clusters (Liu et al. 2022a) and thus excluded from this work. The multi-band detection is performed because, as we show below, the vast majority of the hard-selected sources are also detected in the soft band. Inclusion of the soft photons in these cases can substantially improve the determination of the X-ray source position, which will lead to a more accurate determination of the true hard source counts and hence the likelihood of the hard detection. In addition, the better positional accuracy should aid considerably in the counterpart identification. According to detailed simulations by Liu et al. (2022c), the selection threshold imposed for this catalogue ensures a low fraction (2.5%) of spurious sources.

The resulting hard X-ray sample consists of 246 point-like sources, more than two orders of magnitude fewer than the main sample. The sources' positions within the eFEDS field are shown in Fig. 1, superimposed on the 2.3–5 keV smoothed image. Just 20 of the 246 sources are not also listed in the main catalogue, meaning that they are detected in the hard band but not in the softer 0.2–2.3 keV band used to construct the main catalogue. The lower sensitivity in the hard band can be attributed to two main factors. First, as can be seen in Predehl et al. (2021, see their Fig. 9) there is a pronounced drop in the effective area of eROSITA around ~ 2.3 keV due to M-absorption edges in the gold mirror coating. Above this energy the effective area continues to decline due to the relatively short eROSITA focal length of 1.6m (compared, e.g., to *Chandra* or *XMM-Newton*). Second, at harder X-ray energies, the instrumental background starts to become dominant. This is larger than the pre-flight predictions, partly related to the solar cycle during the first few months after launch (Freyberg et al. 2020; Predehl et al. 2021), and reduces the source detection sensitivity accordingly.

2.3. Optical identifications, classifications and redshifts

Optical counterparts for the hard X-ray sample have been identified by Salvato et al. (2022). A total of three different matching algorithms were applied: the Bayesian NWAY code (Salvato et al. 2018), a maximum likelihood approach (e.g. Sutherland & Saunders 1992; Brusa et al. 2007) and HamStar, a dedicated matching algorithm designed to identify X-ray emitting stars (Schneider et al. 2022). The key datasets to which the X-ray source positions are matched are LS8, which includes forced photometry from unWISE (Lang 2014), and *Gaia* EDR3. The latter also provides parallax and proper motion information that is crucial in distinguishing between Galactic and extragalactic counterparts to the X-ray sources.

A well-defined decision tree is applied to find the most likely counterpart, or identify cases where the counterpart is unlikely or ambiguous. This results in the allocation of a counterpart quality flag between zero and four, described in detail in Salvato et al. (2022). In short, counterpart qualities zero and on are considered to be insecure, three and four to be secure. Counterpart quality two represents cases where the counterpart is ambiguous, and/or where more than one source could contribute to the observed X-ray flux. The results for the eFEDS hard sample are given in Sect. 3.1.

In addition to the counterparts, Salvato et al. (2022) present a compilation of optical spectroscopy of the most likely counterparts to our hard sources, along with photometric–redshift determinations. The vast majority of the optical spectra come from the SDSS telescope (Gunn et al. 2006) using the BOSS spectrographs (Smee et al. 2013). Of these, most are from a dedicated program for X-ray followup within SDSS-IV (Blanton et al. 2017), the SPIDERS program (Dwelly et al. 2017; Comparat et al. 2020). X-ray sources in the eFEDS field have also been targeted explicitly as part of the SDSS-V (Kollmeier et al. 2017) special plates program. The SDSS-V program greatly increases both the spectroscopic completeness and the quality of the data, given that the exposures for the SDSS-V special plates were generally significantly longer. Including a smattering of redshifts from additional programs, a total of 197/246 of our hard sample objects have a spectroscopic redshift as detailed in Table 1. The redshifts used here were derived from the compilation of eFEDS spectroscopic redshifts released as part of SDSS DR18 (Almeida et al. 2023)[1], which have been verified by visual inspection, and superseded those presented by Salvato et al. (2022). The vast majority of spectroscopic objects are extragalactic, with just 12 being spectroscopic stars.

Most of the spectroscopy in the field yields high–confidence redshifts. Three objects have spectra from which no redshift could be determined, but are detected in the radio in the FIRST survey. They are considered candidate BL Lac type objects (see Sect. 4.6 for more discussion), with the lack of a redshift determination being attributed to a lack of spectral features. Reflecting the fact that the hard sources are significantly brighter, the hard sample has very high spectroscopic completeness (80%) compared to the main sample (24%). Several previous hard X-ray surveys have also benefitted from high spectral completeness for the same reason (e.g. Akiyama et al. 2003; Della Ceca et al. 2004; Eckart et al. 2006; Cocchia et al. 2007).

Table 1. Optical spectroscopy.

Origin	Redshifts z	Stellar ($z < 0.001$)	Ref
SDSS	180	2	(1,2)
Gaia-RVS	8	8	–
GAMA	2	–	(3)
6dFGS	2	–	(4)
LAMOST	2	1	–
Simbad	2	1	(5)
2mrs	1	–	(6)
Total	197	12	–

Notes. Where multiple spectra exist of the same object, the table lists the surveys in preference order. References: (1) Blanton et al. (2017); (2) Almeida et al. (2023); (3) Baldry et al. (2018); (4) Jones et al. (2009); (5) Wenger et al. (2000); (6) Huchra et al. (2012).

For the relatively small but significant fraction of our sample for which optical spectroscopy is not available, other information must be used to classify the objects. Salvato et al. (2022) have presented a classification scheme primarily designed to differentiate between Galactic and extragalactic objects, which is particularly important for the current study as we focus on the properties of the latter. Aside from the spectroscopic stars (see above), X-ray source counterparts that have a significant *Gaia* parallax measurement are considered to be securely Galactic, as are all other objects using the 'Hamstar' scheme designed to identify X-ray emitting stars (Schneider et al. 2022). Conversely, objects that are extended in their optical images are assumed to be securely extragalactic. For the remainder, when possible a separation scheme based on optical and mid-IR colors is applied (Salvato et al. 2022) or otherwise an X-ray and mid-IR criterion (Salvato et al. 2018).

Once secure or likely Galactic sources have been identified, we assign photometric redshift estimates to the extragalactic sources without spectroscopic redshifts. These are again discussed and presented in Salvato et al. (2022), and are based on template fitting of the IR-optical-UV spectral energy distribution (SED) using the LePhare code (Ilbert et al. 2006). The photometric redshifts are assigned a 'grade', with a higher grade indicating greater reliability of the photo-z estimate and in particular a lower outlier fraction. Here we adopt `REDSHIFT_GRADE` ≥ 4 in the Salvato et al. catalogue, selecting only objects with either spectroscopic or the most reliable photometric redshift measurements. The latter were selected by comparing the SED-fitting photo-z with an independent measurement using machine learning techniques, specifically a multi-layer perceptron (DNNZ; Nishizawa et al. 2020), and adopting only those measurements where both methods agree. For such cases the photometric redshifts show a low scatter of $\sigma_{\rm NMAD} = 0.043$ and outlier fraction 5.3 per cent (see Salvato et al. 2022, for details). The redshift information for the eFEDS hard sample is provided in Sect. 4.1.

2.4. X-ray spectral fitting

We characterised the spectral properties of our sources both by hardness ratios and full X-ray spectral fitting. We adopted a

---

[1] See also `https://www.sdss.org/dr18/data_access/value-added-catalogs/?vac_id=10001`

Table 2. X-ray spectral models applied to the hard sample.

Name	Energy range (keV)	Description
m0	0.2–8	Single-temperature APEC model with redshift= 0, free kT
m1	0.2–8	Single power law, free Γ, $N_{\rm H}$
m2	0.2–8	Double power law, free Γs, $N_{\rm H}$
m3	0.2–8	Power law plus blackbody, free Γ, kT, $N_{\rm H}$
m4	0.2–8	Same as m1 but fixed Γ = 1.8
m5	2.3–6	Same as m1 but in a narrower band

Notes. In m1, m2, and m3, a log-uniform prior is adopted for $N_{\rm H}$ in the range $4 \times 10^{19} \sim 4 \times 10^{24}$ cm^{-2}, and a Gaussian prior centered at 1.8 with $\sigma = 0.5$ is adopted for Γ in the range $-2 \sim 6$. The appropriate Galactic absorption is applied to all models. More details including other parameter prior ranges are described in Liu et al. (2022b).

standard hardness ratio (HR) definition:

$$HR = (H - S)/(H + S)$$

where H is the flux in the 2.3–5 keV band and S that in the 0.6–2.3 keV band.

A systematic analysis of the X-ray spectra of the eFEDS main sample has been presented by Liu et al. (2022b), who fit a variety of spectral models to determine fluxes and luminosities, as well as physical parameters such as the photon index and $N_{\rm H}$. Although most of the hard sources are included in the main sample, the photon-level data can be different. For example the source positions in the multi-band detected catalogue will in general be subtly different to those in the soft band. We therefore performed an independent spectral analysis for the hard sample separately from the main sample, but using the same method.

Using the eSASS task `srctool`, for each source we calculate a signal-to-noise-ratio optimised source extraction circular region and a source-free background extraction annular region, adopting the same settings as used for the main sample (Liu et al. 2022b). The source and background spectra and the response files in the source regions are then extracted using `srctool`. Before fitting the source spectra, each background spectrum is first fit using a model composed of components extracted from a principal component analysis (PCA) of all the background spectra (described in the appendix of Simmonds et al. 2018). This defines a background model specific to the given source. Then we fit the source and background spectra simultaneously in the 0.2–8 keV energy range (unless otherwise noted) using a source spectral model and the dedicated background spectral model. Few source photons are detected above 8 keV due to the decreasing effective area and consequent dominance of the instrumental background at higher energies. A Bayesian spectral fit is performed with `BXA`[2] (Buchner et al. 2014), which connects `XSPEC` with the `UltraNest`[3] nested sampling package (Buchner 2021). The robust MLFriends nested sampling algorithm (Buchner 2016, 2019) implemented in `UltraNest` explores the model parameter space in a global fashion.

We adopt an absorbed power-law as the baseline model, and modify it according to the requirements of sources with various signal-to-noise ratio, either enriching it with additional components or decreasing the complexity by fixing certain parameters. The models are listed in Table 2 and described in more detail by Liu et al. (2022b). Two double-component models (m2: power-law plus a softer power-law and m3: power-law plus a blackbody component) are applied to describe the potential soft excess. Both of these models are phenomenological in describing the soft excess, which may have different origins and thus spectral shapes in different sources. The soft–excess properties of this sample are discussed in further detail by Waddell et al. (2024). Without the soft–excess component (m1), the power-law slope Γ should be considered as a general description of the broad-band spectral shape. With the soft excess component (m2 and m3), the primary power-law slope can be taken as an intrinsic property of the X-ray emitting corona. The Γ-fixed-power-law model (m4) is the same as the single-power-law model (m1) but with Γ fixed at 1.8. Model 5 (m5) is also the same as model 1 but fitting the 2.3–6 keV spectrum instead of the default 0.2–8 keV band. In addition to the power-law-based models, a hot plasma model (APEC; Smith et al. 2001) (m0), which is appropriate for stars, is used to calculate fluxes of Galactic sources in this sample. In all the models, the Galactic absorption is considered, adopting the total Galactic column density measured from the HI4PI survey (HI4PI Collaboration 2016) and the Schlegel et al. (1998) dust map using the empirical correlation presented by Willingale et al. (2013) (see Liu et al. 2022b, for details).

All the models in Table 2 are fitted to all the spectra. With each model, the observed and absorption-corrected fluxes in the 0.5–2 and 2.3–5 keV band and the intrinsic (absorption-corrected, rest-frame) fluxes and luminosities are calculated in the 0.5–2, 2–10, and a narrow band around 2 keV (1.999–2.001 keV) to provide a monochromatic luminosity at that energy. While not analytical, this last approach makes it simple to calculate this quantity for models with multiple components. In the case of the hard-band fitting (m5), we only calculate the fluxes and luminosities in the hard band (>2 keV). In the case of the APEC stellar model (m0), we only calculate the observed fluxes. Then we choose the most appropriate luminosity measurements as described in Liu et al. (2022b). Unlike the main eFEDS sample that contains many extremely faint sources, almost all the sources in this hard sample have at least moderate S/N. The selection of luminosity measurements can therefore be simplified by omitting special treatment of the faintest sources with `NHclass` of ‘uninformative’, since there are only two such cases. For faint sources with unconstrained Γ (selected based on Kullback-Leibler divergence as described in Liu et al. 2022b), we adopted the ‘Γ-fixed-powerlaw’ model (m4). For the other, brighter sources, we adopted the ‘powerlaw+blackbody’ model (m3) for the unobscured ones and the ‘single-powerlaw’ model (m1) for the obscured ones. The selection is discussed in detail in Liu et al. (2022b). It provides reasonable but not uniformly defined uncertainty measurements. One could also adopt the

---

[2] https://github.com/JohannesBuchner/BXA

[3] https://github.com/JohannesBuchner/UltraNest/

luminosity measurement using one particular model (e.g., m3) if desired. These are provided in the published catalogue (see Appendix A).

2.5. Line measurements and black hole mass estimates

For objects with broad optical and/or UV emission lines, the central black hole mass can be estimated (e.g. Kaspi et al. 2000). The high spectroscopic completeness means such estimates are possible for a large fraction of our sample.

We achieved this using the PyQSOFit code (Guo et al. 2018; Wu & Shen 2022), a python package for χ^2 fitting of optical spectra of quasars. The model consists of several components: a continuum that comprises a power-law, a polynomial component and Balmer continuum; FeII emission in optical and ultraviolet regime; and emission lines that are fitted as single or multiple Gaussians.

After host-galaxy decomposition via the PCA method of Yip et al. (2004) and transformation into the rest-frame, the continuum model is fitted to predefined regions that do not contain strong emission lines. Accurate modelling of the FeII emission is of particular importance, and this was fitted using the following templates in the relevant wavelength range:

- 1000–2200 Å: Vestergaard & Wilkes (2001)
- 2200–3090 Å: Salviander et al. (2007)
- 3090–3500 Å: Tsuzuki et al. (2006)
- optical: Boroson & Green (1992)

The continuum and FeII model is subtracted from the data, leaving only the contribution from emission lines. The emission lines are then fitted using Gaussian functions; the maximum number of Gaussians was predefined for each line component (e.g. three Gaussians for broad Hβ, one Gaussian for narrow Hβ). The output of the code consists of all parameters used to fit the spectrum and an error estimate for each of them based on Monte Carlo simulation.

Using the results, the black hole mass was calculated via:

$$\log\left(\frac{M_{BH}}{M_\odot}\right) = A + B\log\left(\frac{\lambda L_\lambda}{10^{44}\mathrm{erg\ s^{-1}}}\right) + C\log\left(\frac{\mathrm{FWHM}}{\mathrm{km\ s^{-1}}}\right) \qquad (1)$$

with the monochromatic luminosity L_λ at wavelength λ, the full width at half maximum (FWHM) of the broad component of the emission line and the constants A, B and C. The black hole mass was calculated using the Hβ and the MgII emission lines. For the Hβ line, the constants of Vestergaard & Peterson (2006) are used with the monochromatic luminosity at 5100 Å; for MgII, the calibration by Shen & Liu (2012) was selected together with the luminosity at 3000Å. The error of the black–hole mass was calculated via error propagation of the Monte Carlo errors from the fit. These single-epoch black hole mass estimates also carry a systematic uncertainty of around 0.4 dex (Shen 2013). Bolometric luminosities were calculated from the 5100 or 3000 Å monochromatic luminosities adopting the bolometric corrections from the SDSS quasar sample (Richards et al. 2006).

3. Basic properties of the hard sample

While eROSITA is significantly more sensitive in the soft band, the eFEDS data show that the instrument is also able to open up new parameter space for large-area, hard X-ray science compared to previous surveys. Histograms of the 2–10 keV flux and `DET_LIKE` of our sample are shown in Fig. 2. The typical flux of the hard band sources peaks at around (1–2) × 10^{-13} erg cm^{-2} s^{-1}. This is more than 2 orders of magnitude fainter than the HEAO-1 A2 all-sky hard X-ray sample of Piccinotti et al. (1982) and the RXTE all-sky survey of Revnivtsev et al. (2004), which have similar sensitivities below 10 keV.

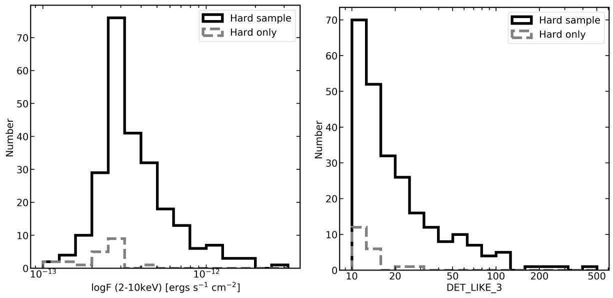

Fig. 2. Histograms of the 2–10 keV X-ray flux (left) and detection likelihood `DET_LIKE` (right) for our sample. Sources detected only in the hard band are shown separately.

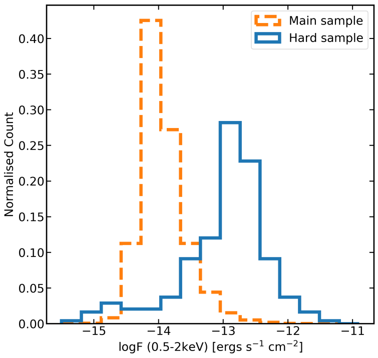

Fig. 3. Normalised histogram of the soft X-ray (0.5–2 keV) flux comparing the main sample (selected in the 0.2–2.3 keV band) with the hard sample (selected in the 2.3–5 keV band). We note that the HBO sources are included in the blue histogram, and will have large uncertainties in their soft X-ray fluxes.

A comparison of the soft X-ray (0.5–2 keV) fluxes between the hard and main sample is shown in Fig. 3. The former samples typically much brighter X-ray fluxes, by more than an order of magnitude, given the higher flux limit overall. There is nonetheless a tail to faint soft X-ray fluxes, mainly due to the sources that are detected primarily in the hard band, some of which may be heavily obscured and therefore have weak soft X-ray emission.

3.1. Optical properties

Turning to the optical identifications, the numbers of counterparts of various types are shown in Table 3. For our hard sample, we find a very high fraction of good counterparts, with 232 sources (∼94%) having a counterpart quality 2 or greater, significantly higher than for the main (soft) sample (81%). This is most likely due to the fact that the typical main sample source is fainter and hence has a fainter counterpart and additional ambiguity in the association.

The assigned source classifications as described in Sect. 2.3 are shown in Table 4. The hard sample has a higher fraction of secure classifications compared to the main sample, reflecting the higher spectroscopic completeness. The fraction of Galactic counterparts is also higher, most likely because on average the hard sample sources are brighter, and the stellar content of hard X-ray samples typically increases with flux.

Table 3. Optical–IR counterpart quality.

Sample	Total	CTP_quality					Secure
		0	1	2	3	4	%
Hard	246	4	11	3	0	228	92
Hard only	20	4	7	1	0	8	40
Main	27 369	1225	1370	2552	1379	20 837	81

Notes. See text for the definition of `CTP_quality`. In the table, we compare the hard and main samples, as well as the sources detected only in the hard band.

Table 4. Source classifications.

Sample	Extragalactic			Galactic		
	Secure	Likely	All	Secure	Likely	All
Hard	181	36	217	14	1	15
Hard (%)	78.0	15.5	93.5	6.0	0.4	6.4
Main (%)	48.4	46.6	95.0	3.3	1.7	5.0

Notes. Classifications are shown for the 232 hard-band sources with `CTP_quality` two or higher with comparison to classifications of the main sample.

Figure 4 shows a comparison between the X-ray flux and optical R and mid-IR W1 magnitudes for the sample, compared to the equivalent data for a representative *Chandra* deep survey, AEGIS-XD (Nandra et al. 2015). The full optical magnitude range for our sample is extremely broad, spanning the range $R_{AB} = 9$–24. The bulk of the AGN population in eFEDS covers a narrower range from $R_{AB} = 15$–22. As is typical of X-ray surveys, a locus is traced by the AGN with a rough anti-correlation between X-ray flux and optical magnitude, with large scatter. X-ray emitting stars are relatively optically bright and can be distinguished by their low X-ray/optical ratios that stand out from the AGN locus. Interestingly, a few of the objects identified as Galactic show ratios more typical of AGN. These could be accretion-powered binaries with enhanced X-ray emission compared to normal stars. Conversely there are some extragalactic objects that are optically as bright as stars.

3.2. Hard-band-only sources and catalogue integrity

As noted earlier, of the 246 sources in the hard sample, 226 are also detected and listed in the main, soft-selected X-ray catalogue of Brunner et al. (2022). Thus 20 of our sources have no significant detection in the softer bands, hereafter referred to as hard-band-only (HBO) sources. If real, these sources must be quite unusual and interesting spectrally, most likely being very heavily obscured, with their soft X-ray emission suppressed by photoelectric absorption hence evading detection in the highly sensitive eROSITA soft bandpass.

On the other hand, the purity of our sample is not expected to be 100%. Specifically, at our chosen likelihood threshold of `DET_LIKE_3`> 10, the simulations of Liu et al. (2022c) suggest a spurious source fraction of approximately 2.5%. Based on this we would expect around 6 of the 246 sources in the hard band not to reflect astrophysical X-ray emission and instead could be random background flucuations. These spurious sources are more likely to be found in the HBO subsample, as the detection in the softer band(s) for the others increases the probability that the X-ray emission has an astrophysical origin. It can be seen from Fig. 2 that the HBO sources tend to be clustered at low detection likelihood (albeit not at particularly faint hard X-ray flux) compared to the remainder of the sample.

The suspicion that some of the HBO sources may be spurious is reinforced by the identification statistics. As can be seen in Table 3 the fraction of the HBO sources without a valid counterpart is much higher than for the whole sample. Indeed, considering the 226 sources that are detected in both the hard and softer bands, >98% of them have a valid counterpart (`CTP_QUALITY` two or greater) while only ~40% of the HBO sources do. Indeed these statistics are entirely consistent with all of the predicted ~6 spurious sources in our sample being HBO sources. On the other hand, the 9 HBO sources with valid optical counterparts seem likely to be real, with the association of the optical source with the X-ray emission lending additional confidence to the X-ray detection itself. We note further that these sources all have an extragalactic classification, which is reassuring given that coronally emitting stars are typically very strong soft X-ray emitters.

3.3. Basic spectral properties

Figure 5 shows the hardness ratio distribution of our sample, split into Galactic and extragalactic sources for sources with reliable classifications. Both span a reasonably wide range of hardness ratio, which in part will reflect the uncertainties in the fluxes from which the HR is calculated. The extragalactic sources show a peak hardness ratio corresponding to an unobscured power law with $\Gamma \sim 1.7$–1.8, typical of AGN, but it can be seen clearly that the extragalactic sources show a tail of hard X-ray sources not present in the stellar sample. This is entirely expected because the extragalactic sample will contain some fraction of obscured AGN (see Sect. 4.3.2), while the stars will generally show soft emission. A very hard X-ray source with a stellar identification would tend to be indicative of an absorbed binary system, where the ID is of a star, and the X-ray emission from accretion onto a compact companion.

4. The AGN subsample

In the remainder of this paper we restrict our discussion to a subsample of the sources that meet all of the following criteria:

- They are contained within the 90%-area region[4], where the exposure is at least 500s (241/246 sources).

---

[4] This exposure depth thresholding excludes the edges of the field, which have a strong exposure gradient (Brunner et al. 2022), and provides a relatively clean selection function for subsequent statistical analysis such as the X-ray luminosity function (Buchner et al., in prep.).

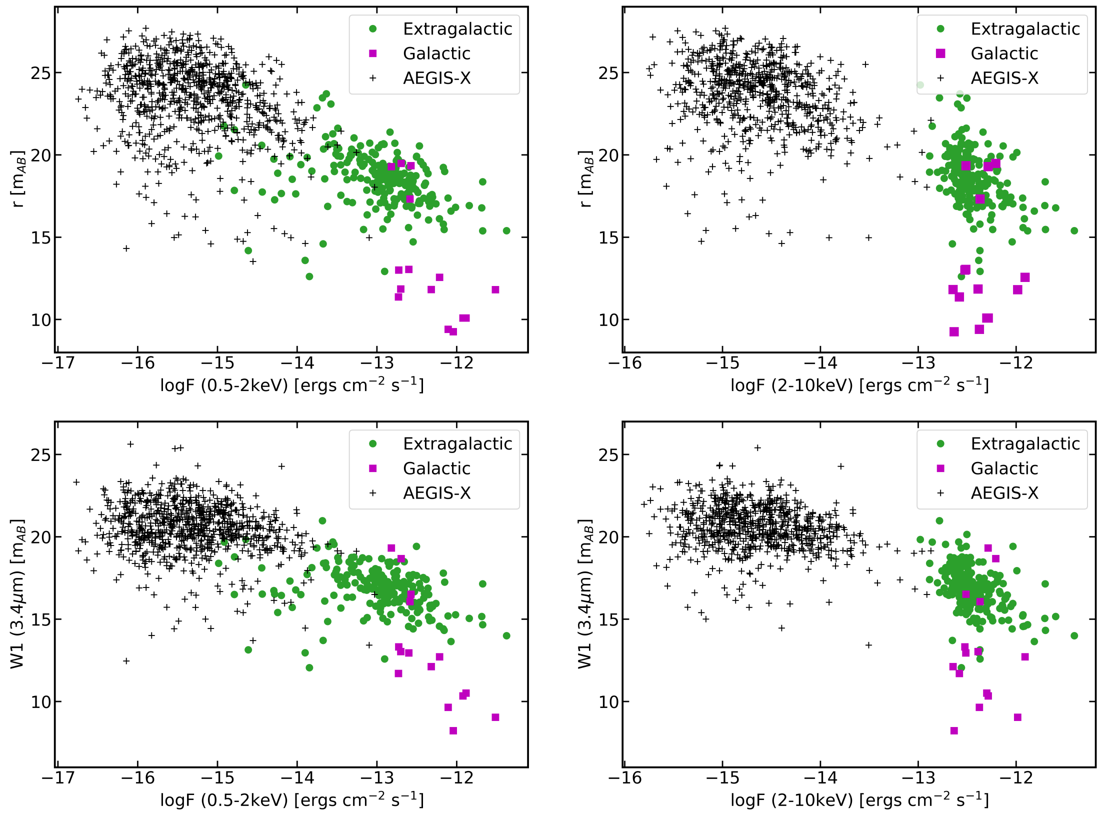

Fig. 4. Legacy survey r-band (uppers panels) and Wise W1 3.4 µm (lower panels) magnitude versus the 0.5–2 keV (left panels) and 2–10 keV (right panels) X-ray flux for the eFEDS hard sample. Sources classified as being extragalactic (green symbols) and Galactic (purple symbols) are shown separately. As a comparison the data for the AEGIS-XD survey (Nandra et al. 2015) are shown (small black symbols), which cover slightly different bands in the optical–IR, specifically Subaru R_c and Spitzer IRAC 3.6 µm.

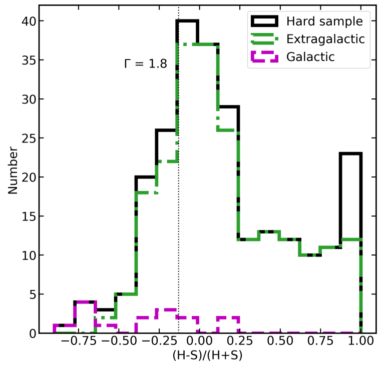

Fig. 5. Histogram of the hardness ratios split between sources classified as Galactic and extragalactic. We note that sources without a high confidence counterpart are not assigned a class in this plot. The extragalactic sources show a tail to large hardness ratio which is suggestive of a population of obscured AGN. Several of these are HBO detections with consequently high values of hardness ratio. The vertical dotted line indicates the hardness ratio expected for an absorbed power law with photon index $\Gamma = 1.8$ and Galactic column density typical of eFEDS of $N_{\rm H} = 3 \times 10^{20}$ cm^{-2}.

- They have counterpart quality two or higher (228/241 sources).
- They are considered secure or likely extragalactic sources (213/228 sources).

This sample is likely to consist overwhelmingly of AGN and we examine their properties in further detail below.

4.1. Redshifts and luminosities

The compilation of spectroscopic redshifts in this field is summarised for the hard sample in Table 1. A total of 179 out of 213 candidate extragalactic sources have a secure spec-z. On top of this spectroscopic sample, an additional 21 sources have a highly reliable photometric redshift determination. We focus our further attention on this subsample of 200 sources, excluding the 13 where the redshift determination is less certain. Fig. 6 (left panel) shows a histogram of the redshift distribution separating the sources into these three categories. The source with the highest reliable redshift measurement in the hard X-ray sample is at $z = 3.2$, spectroscopically confirmed and likely a blazar (see Sect. 4.6). Two objects show high photometric redshift estimates ($z > 3$), but come from the subsample with less reliable redshifts, and we do not consider them to be secure. Henceforth, unless otherwise noted, we plot and consider only the 200/213 (94%) sources that have a spectroscopic or highly reliable photometric redshift.

The right panel of Fig. 6 shows the hard sample redshift distribution compared to that of the main sample. The hard selection clearly samples a significantly lower redshift range than the main sample, with a median redshift $\langle z \rangle = 0.34$ for the former compared to $\langle z \rangle = 0.94$ for the latter. The eROSITA hard selection thus provides an interesting low-z AGN sample for comparison to the higher redshift populations seen in deeper surveys (see Sect. 4.4). Together with the *Swift*-BAT survey (Koss et al. 2022b) eFEDS thus provides information about the low redshift X-ray-selected AGN population, which is poorly sampled by deep X-ray surveys due to their limited area and hence sampled cosmological volume at low-z.

Luminosities for our sample have been derived from the X-ray spectral fits, as described above and in Liu et al. (2022b) and are thus absorption-corrected. The luminosity-redshift relation in Fig. 7 is shown in the soft X-ray (0.5–2 keV) band to facilitate comparison to the main sample. The vast majority of the sample covers the range log $L_{\rm X}$ = 42–45 with a few lower luminosity sources at very low redshift and the ‘standout’ $z = 3.2$ object at

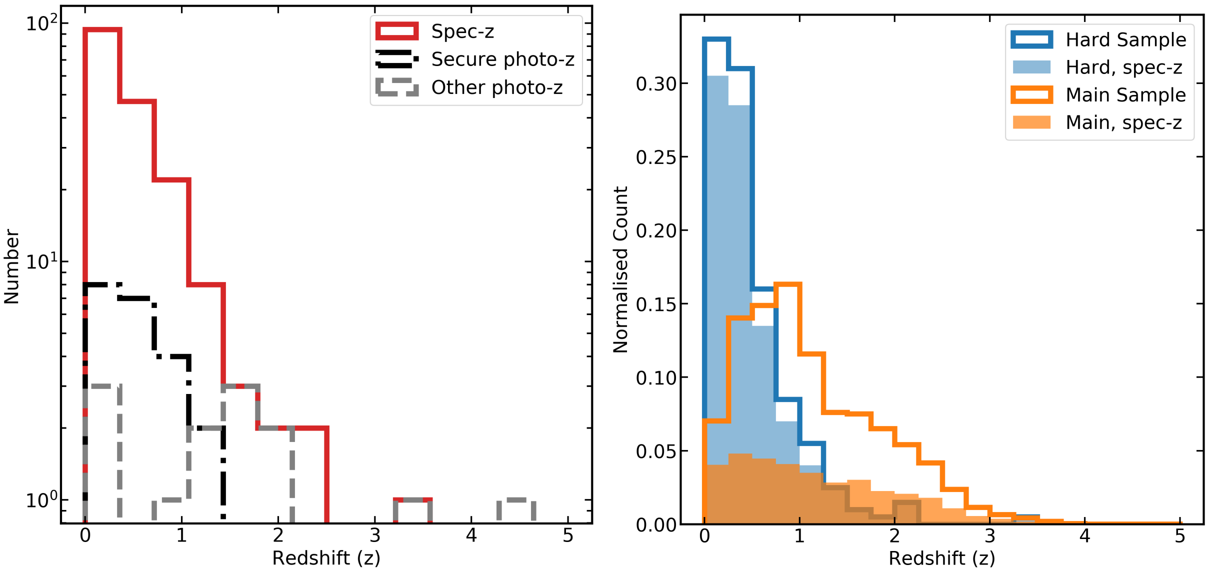

Fig. 6. Redshift distributions. The extragalactic sample is shown in the left panel. Sources with spectroscopic redshift and high reliability photometric redshift are shown separately. The right panel shows the normalised redshift histograms for spectroscopic and highly reliable photo-z comparing the hard and soft samples. The hard X-ray selection yields a relatively local AGN sample, with a median redshift $\langle z \rangle = 0.34$, compared to the main sample that has $\langle z \rangle = 0.94$.

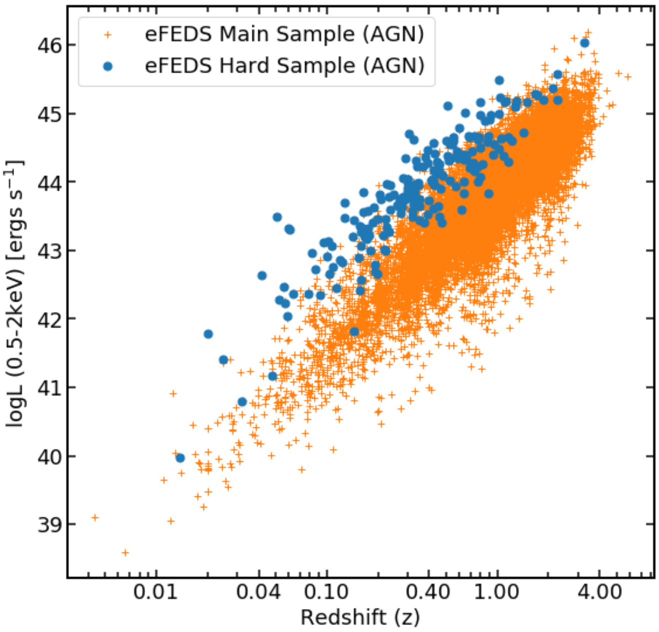

Fig. 7. Soft X-ray (0.5–2 keV) luminosity-redshift relation for the eFEDS hard sample compared to the main sample. The luminosities are corrected for absorption and show the subsamples with either spectroscopic redshift or high quality photometric redshift (see text).

$\log L_X = 46$ being amongst the most luminous even in comparison to the main sample. As expected, the hard selection samples higher luminosities at a given redshift, given the higher flux limit compared to the main sample.

4.2. Optical spectroscopic classifications

For the subsample of our objects that have optical spectroscopy, we are able to provide a basic optical spectral classification. This is most easily achieved by fitting objects with SDSS spectra, for which we have access the spectra themselves. We have visually inspected the 172 spectra with the primary intention of identifying objects with broad lines, predominantly $H\alpha$, $H\beta$, MgII or CIV. A total of 159 objects (~92% of the sample) show evidence for broad emission in at least one of these lines, with the majority of these having prominent broad $H\beta$, MgII and/or CIV. A subset of these objects (25 in total), however, show only broad wings to Hα (which are sometimes only marginally visible) and have no evidence for broad Hβ. We henceforth consider them as optical type 1.9, following the definition of Koss et al. (2022b). Of the 13 objects that show no visual evidence for broad emission in any line, 12 show narrow emission lines and one is an absorption-line galaxy. These objects will be either type 2 AGN or host-galaxy dominated. Thus, despite the hard X-ray selection being sensitive to obscured objects, more than 90% of our sample appear to be optical broad-lined AGN of some kind.

4.3. X-ray spectral properties

The hard X-ray selection and relative brightness of the current sample enable analysis of the spectra with relatively complex models. In particular, the existence of significant hard X-ray counts makes it much easier to infer whether there is line-of-sight absorption of the soft X-rays, or if there is excess emission at low energies above the extrapolation of the power law continuum in the hard X-ray band (i.e. the ‘soft excess’). As a first test, we plot in Fig. 8 the distribution of hardness ratios for three different classes based on the SDSS spectrum. We separate the objects with a measured broad optical line and those without, and plot in addition those sources without optical spectroscopy.

The sources without an optical broad-line detection are more likely to exhibit large hardness ratios indicative of absorption, as are those objects without a spectroscopic redshift. Broad-line objects can also nonetheless exhibit large hardness ratios, and are discussed in Sect. 4.5. We note that the HR is a relatively crude measure of the spectral properties and turn our further attention to the physical properties based on spectral fitting.

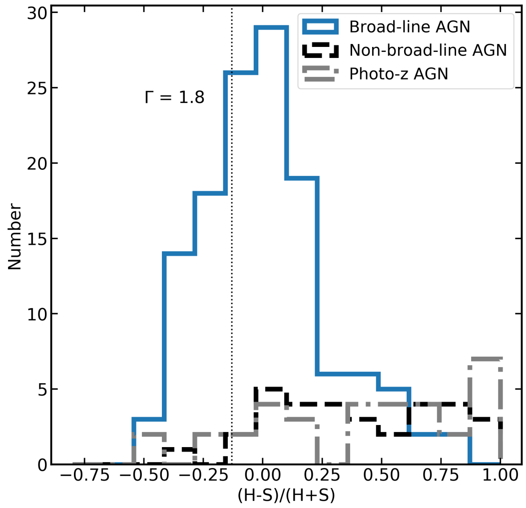

Fig. 8. Hardness ratio distribution for the extragalactic AGN subsample as a function of spectroscopic classification from SDSS. The vertical dotted line indicates the hardness ratio expected for an absorbed power law with photon index Γ = 1.8 and Galactic column density typical of eFEDS of $N_{\rm H} = 3 \times 10^{20}$ cm^{-2}. Objects with broad optical lines (Type 1 classification) dominate the sample, but some of these show large hardness ratios indicative of X-ray absorption. The AGN without broad lines or without spectroscopic classifications show systematically larger values of the hardness ratio, indicating that they are obscured.

4.3.1. Continuum properties

The photon index distribution of the hard sample was determined based on a fit to the spectrum in the full energy range with the 'power-law+blackbody' model (m3 in Table 2). The posterior distribution of Γ is obtained for each source. We combine the posteriors of all the (209) AGN with good redshifts (redshift measurement quality `CTP_REDSHIFT_GRADE`⩾ 3) with a hierarchical bayesian model (HBM) to obtain a sample distribution. Following the approach described in Baronchelli et al. (2020) and Liu et al. (2022b), we adopt both a Gaussian model with a mean μ and a standard deviation σ and a non-parametric, histogram model for the sample distribution. The posterior distribution of the parameters of the sample distribution can be inferred using the PosteriorStacker tool[5], which uses the nested sampling code `UltraNest`. The hierarchical model implicitly allows poorly constrained posteriors to be informed by better-constrained posteriors, as the same model is assumed to describe the distribution for all objects. Figure 9 shows the photon index distribution comparing the main and hard samples.

The main sample, selected in the soft band, has inferred Gaussian distribution centered at Γ = 2.07 ± 0.006 with a intrinsic dispersion (accounting for measurement errors) of 0.24 ± 0.006 (Liu et al. 2022b). For the hard sample, the Gaussian model is found to be centered at 1.83 ± 0.04, significantly harder than the main sample, with a larger dispersion of 0.47 ± 0.04. This is easily understood as sources with very steep intrinsic continua are likely to be missed by the hard selection and vice versa. The histogram model shows that the Γ distribution peaks at 1.9–2 and has a tail at lower Γ values. This low-Γ tail may not reflect the true intrinsic distribution and instead be due to additional spectral complexity (e.g. complex or ionized absorption) that is not considered in our modelling (but see Waddell et al. 2024). Hence the mean intrinsic index in the hard sample may be somewhat softer than that indicated by the mean of the Gaussian HBM.

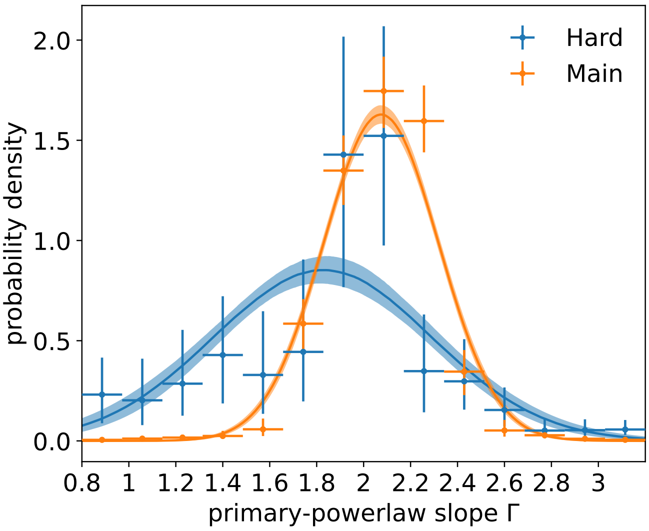

Fig. 9. Distributions of the primary power-law slope in the 'power-law plus blackbody' model (m3) for the hard (blue) and main (orange) AGN sample. The distributions were obtained using the HBM method adopting histogram (points with 1σ error bars) and a Gaussian model (lines with a 1σ range).

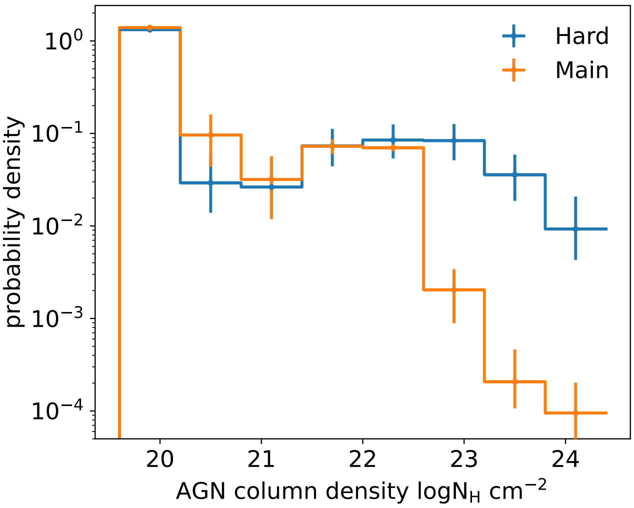

Fig. 10. Distributions of the obscuring column density in the 'single-power-law' model (m1) for the hard AGN sample (blue) and the main AGN sample (orange), obtained using the HBM method. The 1σ error bar is plotted on the histogram.

4.3.2. Obscuration

We used the same HBM method described in Sect. 4.3.1 to infer the sample distribution of AGN column density $N_{\rm H}$ from the posteriors measured with the 'single-power-law' model (m1) of all the AGN with good redshifts. We adopted only the histogram model and not the Gaussian model because in practice the shape of the distribution is very different from a Gaussian. We used the single-power-law model rather than the double-component models because in the obscured cases a soft–excess component can be strongly degenerate with the AGN obscuration, and our data quality does not allow constraints on both simultaneously. Figure 10 compares the $N_{\rm H}$ distribution for the main and hard

---

[5] https://github.com/JohannesBuchner/PosteriorStacker

samples. In both cases, the distributions show a dominant bin at the lower boundary $\sim 10^{20}\mathrm{cm}^{-2}$, showing that the majority of sources in both the hard and main samples are unobscured.

Both the main and the hard sample N_H distribution show a bi-modality. This can be quantified by drawing a line between the fractions in the $\sim 10^{20}\mathrm{cm}^{-2}$ bin and the $\sim 10^{22}\mathrm{cm}^{-2}$ bin, and noticing that both the $\sim 10^{20.5}\mathrm{cm}^{-2}$ and the $\sim 10^{21}\mathrm{cm}^{-2}$ bins are 10σ lower, indicating a dip and thus multi-modality (Hartigan & Hartigan 1985). Therefore, we have evidence that there is a low-column density mode $<10^{20.5}\mathrm{cm}^{-2}$ and a high-column density mode $\sim 10^{22}\mathrm{cm}^{-2}$. The latter can be associated with nuclear or host galaxy obscuration (Buchner et al. 2017; Buchner & Bauer 2017).

The distributions diverge at high N_H. The main sample, selected in the soft band (0.2–2.3 keV), has a very low fraction of obscured sources with $N_\mathrm{H} > 10^{22}$ cm^{-2} (4%; Liu et al. 2022b) in the HBM-inferred distribution, reflecting the strong selection bias against obscured sources. For the hard sample, the fraction above 10^{22} cm^{-2} is much higher (13%). Even more highly obscured sources with $N_\mathrm{H} > 10^{23}$ cm^{-2} are almost absent from the main sample, while in the hard sample the numbers are significant, with a probability of around 4% of having such a high N_H. This is roughly in line with expectations. At the median redshift of $z = 0.34$ a column density of 10^{22} cm^{-2} only suppresses the 2.3–5 keV flux by around 5 per cent, whereas the flux is reduced by 40 per cent at a column of $N_\mathrm{H} = 10^{23}$ cm^{-2}, which will start impacting significantly on source detectability.

To define an ‘obscured’ subsample, we adopt the same definition as Liu et al. (2022b). Based on the posterior Probability Distribution Function (PDF) for N_H obtained with the single-power-law model (m1), Liu et al. (2022b), we divide the N_H measurements into four classes (`NHclass`): (1) uninformative, (2) unobscured, (3) mildly measured, and (4) well-measured. The posterior median $\mathrm{N_H}$ value (`lognH_Med_m1`) is invalid in the first two cases. Following Liu et al. (2022b), we adopt the criterion `NHclass`$\geqslant$ 3 and `lognH_Med_m1`> 21.5 and select 36 obscured AGN, which comprises 18% of the hard AGN sample (200). The largest measured value us `lognH_Med_m1`= 24.0.

4.3.3. Soft excesses

The hard-selected sample has by selection a defined hard X-ray continuum and, combined with the high soft X-ray sensitivity of eROSITA in the soft X-ray band, is ideal to search for so-called soft excess emission. The origin of this component is still debated, as it can arise, for example, from a second, cooler coronal component, ionised disc reflection, or it can even be an artefact of complex soft X-ray absorption. In the present work we restrict ourselves to relatively simple modelling of the soft excess emission.

The standard fits shown in Table 2 include both a double power law (model 2) and a power law plus black body. We can therefore identify sources with a soft excess by comparing the Bayesian evidence of these models to a single power law. Specifically we use the criterion $\log Z_{m2} - \log Z_{m1} > 1$, which selects 17 sources better fit with a double power law, or $\log Z_{m3} - \log Z_{m1} > 1$, which yields seven sources fit better with a power law plus black body. The seven sources with apparent black body soft excesses are a subset of the 17 power law soft excesses, indicating that the latter model is better and more sensitive for soft excess detection. Sources with a soft excess comprise about 10% of the AGN sample.

4.4. Black hole masses and Eddington ratios

As discussed above, black hole masses have been estimated using the single-epoch virial method for the objects in our sample exhibiting a broad Hβ, MgII or CIV line, in other words the spectroscopic type-1 AGN. For the 134 AGN that show broad emission at Hβ or bluewards thereof, we calculated the black hole masses and other derived parameters with optical spectral fitting using pyQSOFit (see Sect. 4.4). We did not consider Hα-based masses (e.g. Greene & Ho 2005) because there are indications that these may be biased and/or unreliable in Seyfert 1 type AGN.

Of the 200 AGN in the sample with reliable redshift, 179 are spectroscopic. We restricted our black hole analysis to the 172 objects with spectra originating from SDSS, to which we have full access and for which we have optical spectral fitting results based on PyQSOFit as described in Wu & Shen (2022) and Sect. 2.5.

As described there, for type 1 objects the black hole masses and bolometric luminosities can be estimated using the line widths and optical–UV continuum, and the accretion rate relative to Eddington can also be estimated from these quantities. As we are interested in the latter derived quantity, we follow Waddell et al. (2024) in sub-selecting only objects with a constrained Eddington ratio. This results in a subsample of 154 sources. The distributions of redshift, black hole mass, bolometric luminosity and Eddington ratio for this black hole mass subsample are shown in Fig. 11. This subsample has a median redshift of $z_\mathrm{med} = 0.39$ and median luminosity $\log L_\mathrm{bol,med} = 45.3$.

The black hole masses cover $\log M_\mathrm{BH} = 7$–10, peaking in the middle of this range with a median $\log M_\mathrm{BH,med} = 8.6$. The objects with Mg II-derived masses are at the top end of the mass range. This is unsurprising, as they are the highest redshift and hence are amongst the highest luminosity sources in this flux-limited sample. The Eddington ratios cover a very broad range, from $\sim 10^{-3}$ up to the Eddington limit. Certainly, eFEDS samples objects at the high ends of both the mass and accretion rate distributions. We note, however, that there are significant uncertainties on our estimated quantities, so the most extreme cases should be treated cautiously. In addition, the objects with the highest bolometric luminosities in the eFEDS sample are the handful of blazars (see Sect. 4.6 and, for example, Fig. 11). We caution that in these objects, the optical–UV continuum may be contaminated by jet emission that could lead to an overestimate of the bolometric luminosity and quantities derived therefrom (mass and accretion rate). However, as there are relatively few of these in our sample we do not consider this a major effect.

To place the eFEDS results in context, we show in Fig 11 the corresponding distributions from the work of Suh et al. (2020), from the *Chandra* COSMOS legacy survey. The latter samples a significantly higher redshift range, with $z_\mathrm{med} = 1.58$, but due to the higher sensitivity of the deep *Chandra* observations in this region the two surveys sample a similar limiting luminosity at their median redshift, around $\log L_{2-10} = 44$ in the rest frame. It is therefore of interest to compare the two samples in relation to possible evolution of the AGN population.

From Fig. 11 we can see that the black hole mass range in the two samples is rather similar, covering the same range and with a remarkably similar median, with $\log M_\mathrm{BH,med} = 8.55$ in COSMOS compared to 8.63 for non-blazars in eFEDS. A K-S test reveals no significant difference between the distributions, with false probability $p = 0.08$. In contrast, the Eddington ratio distributions are dramatically different with the K-S probability of them being the same $<4 \times 10^{-5}$ (once again excluding blazars).

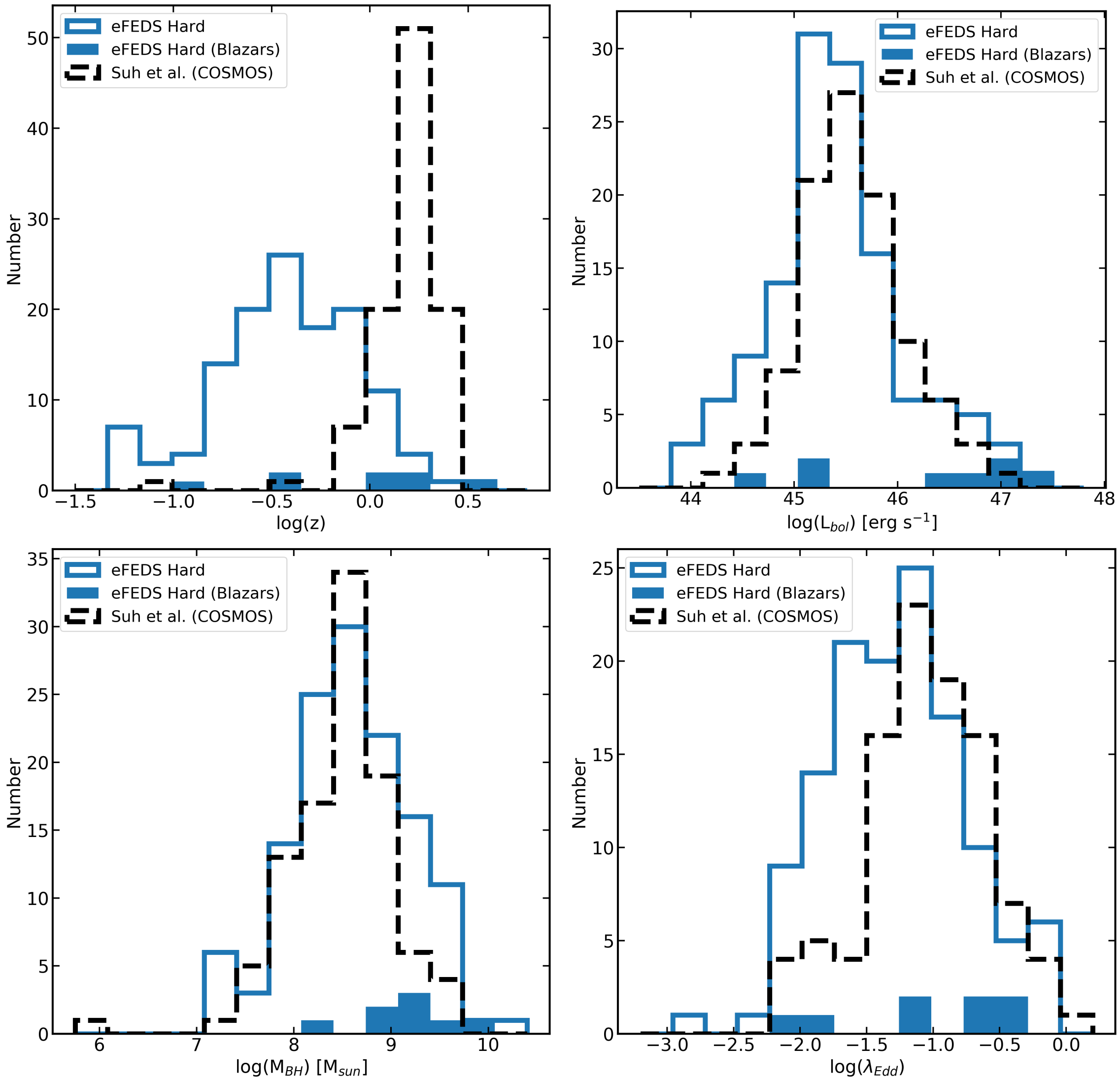

Fig. 11. Distribution of the redshift (top left), bolometric luminosity (top right), black hole mass (bottom left) and Eddington ratio (bottom right) for spectroscopically confirmed type 1 AGN in the eFEDS hard sample, shown in blue. The dotted black histogram shows a comparison sample from the *Chandra* deep survey in the COSMOS field (Suh et al. 2020).

The median Eddington ratio for eFEDS ($\lambda_{\rm Edd,med}$ = 0.03) is about three times lower than that in COSMOS ($\lambda_{\rm Edd,med}$ = 0.09).

4.5. X-ray absorbed type 1 AGN

With a combination of relatively deep and sensitive soft X-ray data, as well as comprehensive follow-up optical spectroscopy, we are able simultaneously to classify the objects in our sample optically and measure their absorption in the X-ray. A particularly interesting population in this regard are X-ray obscured type 1 AGN (e.g. Page et al. 2001; Brusa et al. 2003; Page et al. 2011), that is, objects that show broad optical lines but exhibit soft X-ray absorption. The demographics of this population have been explored, for example, in Merloni et al. (2014).

In the very simplest unification scenarios, this is not expected, because the same gas that absorbs the X-rays should contain dust that extinguishes the optical broad lines. On the other hand, there is evidence that the obscuring material is clumpy (e.g. Nenkova et al. 2008; Markowitz et al. 2014), that the broad-line clouds can have a complex geometry (Maiolino et al. 2010) and that there may be substantial departures from normal gas-to-dust ratios (Maiolino et al. 2001). The broad lines and AGN continuum may also be seen only in scattered light (Antonucci & Miller 1985; Alexandroff et al. 2018; Assef et al. 2020). An interesting possibility is that the X-ray absorbing gas is dust-free, which would be the case if it is close to the central engine within the dust sublimation radius. If so, the gas may be significantly ionised and in the form of ‘warm absorbers’ (Halpern 1984; Yaqoob et al. 1989) that are, in turn, associated with ionised winds (e.g. Kaastra et al. 2000). Evidence for significant X-ray absorption in type 1 AGN has also been found in broad absorption line quasars (e.g. Gallagher et al. 2006; Gibson et al. 2009), which have direct evidence for strong outflows.

Our hard X-ray sample is dominated by broad-line AGN, but nonetheless contains a number of objects with significant soft X-ray absorption. Considering the 154 objects in the ‘black hole mass’ sample as defined in Sect. 4.4 – which by definition must have a visible and constrained broad optical line – we find that four also satisfy the criterion of being obscured by a column of $\log N_{\rm H} > 21.5$ as defined in Sect. 4.3.2. These obscured type 1 AGN are identified in black hole mass-accretion rate parameter space in Fig. 12. Naively, one might expect these absorbers

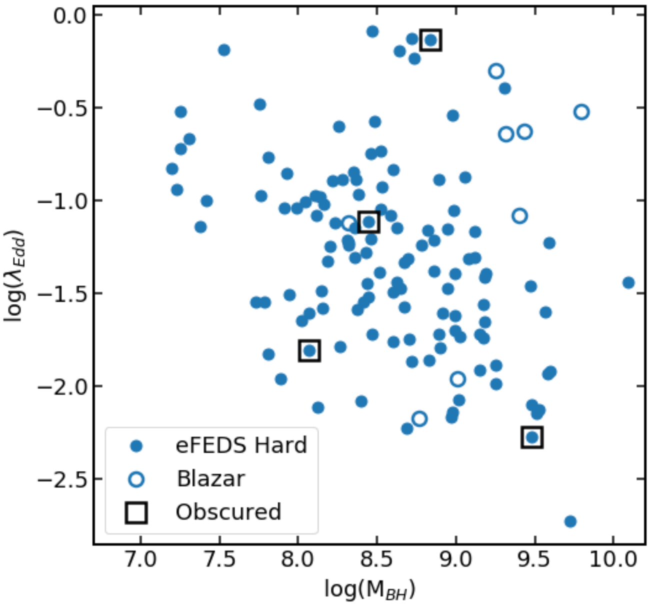

Fig. 12. Black hole mass versus Eddington ratio for the type 1 AGN sample. Type 1 AGN that show evidence for significant absorption, having an NHclass of 3 or 4 and a column density greater than $10^{21.5}$ cm^{-2}, are indicated with black squares.

to be seen in AGN with high accretion rates where, close to the Eddington ratio, radiation pressure drives an outflow (e.g. Fabian et al. 2008; Ricci et al. 2017). In practice they show a wide range of Eddington ratios. None of the objects shows Broad Absorption Line (BAL) signatures in the Sloan spectra, but only one (at z=2.25) is within the redshift range where classical UV BAL signatures would be evident.

In addition to the black hole mass subsample, as noted in Sect. 4.2, Seyfert 1.9 galaxies comprise a substantial subset of our sample. Several of these (6/25) also show significant soft X-ray absorption but this is unsurprising given the evidence for line-of-sight obscuration based on the suppression of optical broad lines bluewards of Hα.

4.6. Blazars

Due to the large area of the eFEDS survey it is sensitive to rare AGN such as those at the highest luminosities. In some fraction of these, the luminosity is enhanced due to the presence of a relativistic jet whose emission is Doppler boosted for sightlines close to the jet axis. Such blazars can be identified via strong radio and/or Gamma-ray emission. A more detailed study of the blazars in eFEDS is given in Collmar et al. (in prep), but here we highlight the sources in the hard X-ray sample that are likely to host strong emission from a relativistic jet. Confirmed blazars and blazar candidates have been identified by cross-correlating the hard sample with catalogues of blazars identified via their radio and/or gamma-ray emission.

As input catalogs we used the following: the Fermi Large Area Telescope Fourth Source Catalog (4GL; Abdollahi et al. 2020); the ROMA-BZCAT Multifrequency Catalog of Blazars (Massaro et al. 2015); the 3HSP catalogue of extreme and high-synchrotron peaked blazars (Chang et al. 2019); the *Swift*-XRT catalogue of blazars (Giommi et al. 2019); the Blazar Radio and Optical Survey (BROS; Itoh et al. 2020) and the WISE Blazar-like Radio-Loud Sources catalogue (D'Abrusco et al. 2019).

To select blazars or blazar candidates we searched for a positional coincidence of < 15 arcseconds and cross-checked the identifications with the eFEDS counterpart catalogue of Salvato et al. (2022).

There are 15 such objects in our sample, as detailed in Table 5, of which two are outside the 90% area region, both BL Lac type objects. Of the remaining 13, 7 are flat spectrum radio quasars, all spectroscopically confirmed, two are BL Lac type objects and four are candidate blazars or of unknown type. Our own visual examination of the SDSS spectra largely confirms the literature classifications. The four BL Lac type objects show largely featureless blue continua, with only one (4FGL J0831.8+0429) showing weak lines sufficient for a redshift determination. The flat spectrum radio quasars (FSRQ) generally exhibit Quasi-Stellar Object (QSO) broad emission lines, but two show optical properties indicating obscuration, with 5BZQ J0924+0309 having the optical spectrum of a Seyfert 1.9 and WIBRaLS2 J092203.20-004443.3, listed as a FSRQ candidate, having narrow lines indicative of a type-II QSO classification. A final noteworthy object spectroscopically is 3HSPJ093303.0+045235, which presents as an absorption-line galaxy with no AGN emission lines, but a possibly enhanced blue continuum. This is plausibly a BL-Lac type object in which the non-thermal jet emission is subdominant in the optical compared to the host galaxy.

A particularly extreme object amongst these and indeed the eFEDS hard sample as a whole is eFEDS J090915.8+035442, identified with the blazar candidate BROS J0909.2+0354 (Itoh et al. 2020). This is both the highest redshift and the highest luminosity source in the sample. It has optical broad lines, but a measured absorption column of $\log N_{\rm H} = 10^{21.4}$ cm^{-2}, almost satisfying our criterion for being obscured. This absorption may not be intrinsic to the quasar, but instead may originate in the intergalactic medium (Arcodia et al. 2018).

5. Discussion

In this paper we have presented the sample of hard X-ray-selected objects detected in 2.3–5 keV band in the eFEDS survey. At the time the data were acquired, the 140 deg^2 of coverage provided by eFEDS constituted the largest contiguous X-ray survey above 2 keV, now surpassed only by the all-sky eRASSs (Merloni et al. 2024). The large area and cosmological volume probed, together with comprehensive supporting data particularly in terms of spectroscopy, have yielded new insights into the hard X-ray source populations and this hard X-ray parent sample can also be used to select objects or subsamples or particular interest for further detailed study (e.g. Brusa et al. 2022; Waddell et al. 2024).

5.1. The hard X-ray sky seen by eROSITA

Due to the short focal length and thus soft response of eROSITA, the hard X-ray sensitivity is considerably less than in the main (0.2–2.3 keV) eROSITA detection band, with the sample size being around 100 times smaller. The 246 hard X-ray sources in our sample have been identified optically and classified according to whether they are Galactic or extragalactic. The vast majority (90 %) are in the latter category and are overwhelmingly AGN. Extensive spectroscopic coverage in the field thanks mainly to the SDSS-IV and SDSS-V surveys yields a high spectroscopic redshift completeness for our sample of around 80%,

Table 5. Blazars and blazar candidates identified in the hard sample.

Name	SRCID	DET_LIKE_3	Name	z	z_orig	Class
eFEDS J083148.9+042939 $^{(a)}$	65	29.8	4FGL J0831.8+0429	0.174	SDSS	bll
eFEDS J083949.5+010427	112	57.1	4FGL J0839.8+0105	1.124	SDSS	fsrq
eFEDS J085301.2-015049	148	41.7	5BZQ J0853-0150	1.498	Simbad	fsrq
eFEDS J085920.5+004711	19	45.4	4FGL J0859.2+0047	1.47	photz	bll
eFEDS J090111.8+044900	1116	10.8	5BZQ J0901+0448	1.862	SDSS	fsrq
eFEDS J090910.2+012135	25	68.4	4FGL J0909.1+0121	1.024	SDSS	fsrq
eFEDS J090915.8+035442	78	75.1	BROS J0909.2+0354	3.262	SDSS	bcuc
eFEDS J090939.9+020005	354	15.4	4FGL J0909.6+0159	0.15	photz	bll
eFEDS J091408.2-015944	10	61.9	4FGL J0914.1-0202	1.15	photz	bcu
eFEDS J091437.8+024558	55	41.9	4FGL J0914.4+0249	0.427	SDSS	fsrq
eFEDS J092203.5-004442	16 185	11.3	WIBRaLS2 J092203.20-004443.3	0.576	SDSS	fsrqc
eFEDS J092400.9+053345 $^{(a)}$	20	50.4	4FGL J0924.0+0534	1.99	photz	bll
eFEDS J092414.7+030859	23	114.1	5BZQ J0924+0309	0.128	SDSS	fsrq
eFEDS J092507.8+001913	457	19.9	5BZQ J0925+0019	1.721	SDSS	fsrq
eFEDS J093303.3+045235	41	27.9	3HSPJ093303.0+045235	0.378	SDSS	bcu

Notes. Class definition are: bll= BL Lac; fsrq = Flat Spectrum Radio Quasar; fsrqc = fsrq candidate; bcu = Unclassified blazar; bcuc = Unclassified blazar candidate. $^{(a)}$Outside Area90.

with the remaining sources having photometric redshift estimates. This high redshift completeness at bright fluxes is in part what distinguishes eFEDS from larger, non-contiguous wide field surveys such as Champ, the *Chandra* Source Catalogue and 4XMM (Green et al. 2004; Evans et al. 2010; Webb et al. 2020). The redshift distribution shows that the eFEDS hard survey yields a relatively nearby population of extragalactic sources, with median redshift $\langle z \rangle = 0.34$, compared to the eFEDS soft X-ray sample or deeper pencil-beam surveys with *Chandra* and *XMM-Newton*. The hard survey therefore provides an interesting lower-redshift baseline for evolutionary studies of AGN. The extensive optical spectroscopy in the field shows that the overwhelming majority of the objects in the eFEDS hard X-ray sample are type 1 AGN, despite the hard X-ray selection being sensitive to at least moderately obscured objects. Similar effects have been found also in previous hard X-ray surveys at relatively bright fluxes (La Franca et al. 2002; Della Ceca et al. 2008, e.g.)

An interesting subclass of objects are the optically bright extragalactic sources that stand out somewhat from the general population in Fig. 4. For example our extragalactic (AGN) subsample contains six objects with $r < 15$. Optical spectroscopy show that these are all very low redshift galaxies with $z < 0.05$. In principle these may be normal galaxies whose X-ray emission is dominated by binary populations and hot gas emission (see Vulic et al. 2022, for a discussion of the normal galaxies in eFEDS) but in reality most of these hard X-ray-selected sources show AGN signatures including broad Hα and their X-ray luminosities are also indicative of AGN activity, with $\log L_X > 41$. One such object, eFEDS J085547.9+004747, is a HBO detected object and one of the most obscured objects in the entire sample, with $\log N_H = 23.3$ for an absorbed power law fit. Despite our concern that many HBO sources could be spurious, this object is very well detected with `DET_LIKE_3=30.6` and a confirmatory detection in the *Swift* 105-month catalogue (Oh et al. 2018).

5.2. X-ray spectral properties of the hard sample

X-ray spectral analysis of the hard sources shows that a significant fraction exhibit soft X-ray absorption, with the survey having some sensitivity to column densities as high as $N_H = 10^{24}\mathrm{cm}^{-2}$. eROSITA hard samples can therefore be used to explore the demographics of the (Compton-thin) obscured populations. We observe a dip in the column density distribution near $N_H \sim 10^{20.5}\mathrm{cm}^{-2}$. This may indicate that the medium around AGN is not a single, continuous density distribution from 10^{20} to $10^{23}\mathrm{cm}^{-2}$ and above, but composed of discrete clumps of a significant, typical column density $N_H \sim 10^{22}\mathrm{cm}^{-2}$ (see, for example Buchner & Bauer 2017; Buchner 2019), with unobscured sight-lines in between. A bi-modality has also been seen in the optical obscuration (Assef et al. 2013).

At column densities of $N_H > 10^{22}$ cm^{-2}, the selection function needs to be taken into account carefully, given that the survey will become increasingly incomplete for higher absorbing columns. After accounting for absorption, the hard sample exhibits similar intrinsic photon indices as the eROSITA soft sample, but with a tail to flat photon indices that might be indicative of un-modelled soft X-ray spectral complexity, including ionised absorbers, which may not be correctly matched by the cold absorption model employed here.

This conclusion is supported by the fact that a small but significant fraction of our sources exhibit soft X-ray absorption, while being optical type-1s (see, e.g. Brusa et al. 2003; Page et al. 2011; Merloni et al. 2014). One explanation for this is that the absorber is ionised and dust-free, presumably being located close to the origin of the nuclear ionising radiation and well within the dust sublimation radius. Ionised or warm absorbers have been shown via high resolution X-ray spectroscopy to take the form of outflows (e.g. Kaastra et al. 2000; Kaspi et al. 2002) and such outflows could be an important component of the accreting system as well as having wider influence. Naively, one might expect these winds to be launched at the highest accretion rates, but as shown in Fig. 12 the absorbed type 1 AGN are preferentially seen at more modest accretion rates. This is in concurrence with the conclusions of Liu et al. (2018) based on the XMM-XXL field and the more detailed analysis of the eFEDS hard sample data presented in Waddell et al. (2024). The most likely overall explanation for the lack of warm absorbers at the highest accretion rates is that the gas becomes over-ionized, decreasing the efficiency of radiative line-driving (Proga et al. 2000). It should also be noted that the exact relationship between accretion rate and the launching of winds could be complicated by factors such as geometry and the presence or absence of dust (e.g. Fabian et al. 2008; Ricci et al. 2017). Our result is also somewhat in tension with theoretical models of ‘slim disks’ (Abramowicz et al. 1988) which predict strong winds at high accretion rate (e.g. Dotan & Shaviv 2011). These effects may only apply at super-Eddington rates which are not sampled here (see Fig. 11).

Soft X-ray spectral complexity of the opposite kind is also evident in the form of a soft excess, detected in around 10% of the extragalactic sources. Our modelling indicates that this has a power law, rather than black body form. The origin of the soft excess emission in AGN is still debated, with possibilities including a secondary corona, complex absorption or relativistic X-ray reflection from an ionised accretion disk. The spectral modelling favours the warm corona interpretation. Again, the above results confirm the more sophisticated analysis of the soft X-ray complexity of the eFEDS hard X-ray sample excesses presented in Waddell et al. (2024).

5.3. AGN evolution and downsizing

The relatively local nature of the eFEDS hard sample offers an interesting baseline to be compared to deeper pencil beam surveys, with the large area of eFEDS offering sufficient cosmological volume to provide a fair sample of the low redshift Universe. In this work, in particular, we have compared the black hole mass and accretion rate distributions between eFEDS and the deeper COSMOS survey. Fortuitously, the luminosity limit of eFEDS and COSMOS observations at their respective median redshift is similar, as is their rest frame selection bandpass, and they also yield similar sample sizes.

We find a remarkable similarity between the black hole mass distributions, but with a clear difference in the accretion rate distributions, in the sense that the typical black hole growth rate relative to Eddington is about a factor three lower in eFEDS than in COSMOS. This result is of particular interest given that the global accretion rate density has declined substantially between the two cosmic epochs sampled by the COSMOS and eFEDS samples. Under the assumption that the populations sampled by these surveys are representative of the overall AGN populations and hence the global accretion rate it suggests that the decline in accretion rate is due primarily to a reduction in the typical fuelling rate of black holes, rather than a ‘downsizing’ effect where the sites of active accretion occur in objects with a lower typical black hole mass.

This general effect is similar to that seen in work that analyses the evolution of the specific accretion rate distribution of AGN over cosmic time, as traced by the ratio of the X-ray luminosity to host stellar mass (e.g. Aird et al. 2012; Bongiorno et al. 2016; Georgakakis et al. 2017). Based on the extensive optical spectroscopy in our field, it has been possible here to calculate the accretion rate more directly via the line width and black hole mass estimates. Our finding of a lack of downsizing effect in the overall black hole populations contrasts somewhat with some previous studies of optical quasars, which do see such an effect (e.g. Kelly & Shen 2013; Schulze et al. 2015). The difference may be due to the selection band, but full understanding requires careful modelling of the selection effects (Trump et al. 2015; Jones et al. 2016).

6. Conclusions and outlook

We have presented the properties of a sample of X-ray sources selected in the relatively hard 2.3–5 keV band from the eROSITA eFEDS survey. The sample of 246 sources is around two orders of magnitude smaller than the main soft X-ray-selected eROSITA catalogue in this region, reflecting the lower effective area and higher background of the instrument in this band. The hard sample consists overwhelmingly of extragalactic sources and, more specifically, AGN, with a small fraction of stars. Being relatively bright and benefiting from extensive dedicated spectroscopy from the SDSS-IV and SDSS-V surveys, the sample has a very high spectroscopic completeness (80%) which increases to ~94% when only the extragalctic AGN subsample is considered, and enables a number of properties to be explored in detail:

1. The hard-selected AGN cover a wide luminosity and redshift range up to $z \sim 3$, but the selection predominantly results in a relatively nearby sample with $\langle z \rangle \sim 0.3$, which is interesting to compare to higher redshift objects in the main sample and in deeper surveys.
2. The intrinsic power law index appears similar, if perhaps slightly harder, than the main eFEDS sample.
3. The hard selection yields a small but significant subsample of highly obscured AGN, with $\log N_{\rm H} > 23$. We characterised the column density distribution from $\log N_{\rm H} = 20{-}22$ in fine detail.
4. The hardest sources in the sample tend to be optically unclassified spectroscopically and are probably obscured, type 2 AGN. On the other hand a significant subsample (~10%) of the optical broad-line AGN are also X-ray obscured. These may be warm absorbers with an outflowing nuclear wind, and they are observed preferentially at low Eddington ratios (see also Waddell et al. 2024).
5. Several of the brightest and most luminous sources in our sample are blazars, predominantly flat-spectrum radio quasars and many of them are also γ-ray emitters.
6. For the objects with optical broad lines, we were able to estimate black hole masses and accretion rates. When comparing to a similar sample of high redshift objects in the COSMOS field, we found a very similar distribution of black hole masses but significantly lower Eddington ratios (by a factor ~3) in the lower redshift eFEDS sample. This provides important clues as to the origin of the decrease in the overall accretion luminosity of the Universe since $z \sim 1-2$.

As mentioned earlier, eFEDS was designed as a precursor to the eight-pass eRASS:8 survey and intended to demonstrate the power and potential of the full survey. With the exception of the XMM-Slew survey (Saxton et al. 2008), previous all-sky or near all-sky surveys in the hard band have had to rely on non-imaging instruments. Notable examples include the HEAO-1 A2 all-sky survey catalogue (Rothschild et al. 1979), the RXTE all-sky survey (Revnivtsev et al. 2004) and the *Swift*-BAT survey (BASS; Oh et al. 2018; Koss et al. 2022b). With resulting AGN catalogues presented by, for example, Piccinotti et al. (1982) for HEAO-1 A2, Sazonov & Revnivtsev (2004) for RXTE, and Ricci et al. (2017) and Koss et al. (2022a) for BASS. The luminosity-redshift relation of eFEDS is compared to some of these surveys in Fig. 13, which clearly shows the superior sensitivity even of the single-pass eRASS1 survey (Merloni et al. 2024) compared to previous hard X-ray all-sky surveys, which is effectively around two orders of magnitude deeper than HEAO-1 (or the similar RXTE all-sky survey) in the standard 2-10 keV bandpass.

Arguably the most interesting comparison survey from the point of view of AGN science is the *Swift*-BAT survey (Oh et al. 2018) which is highly spectroscopically complete (Koss et al. 2017, 2022b) and has given important new insights into the local AGN population. The harder bandpass of *Swift* BAT

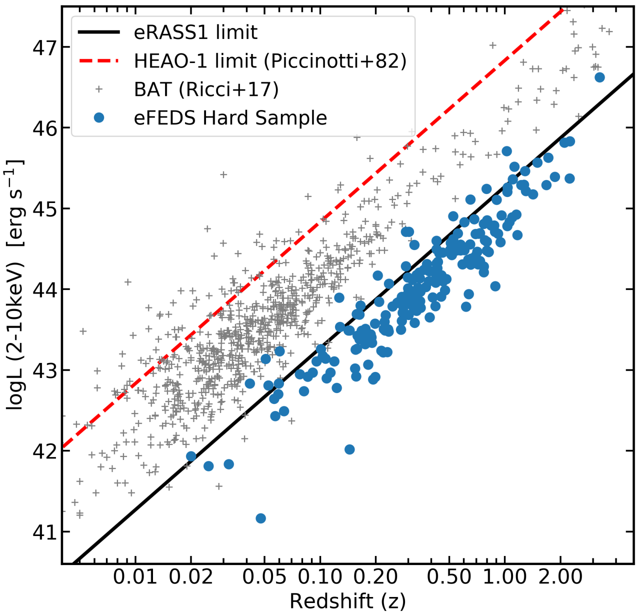

Fig. 13. Luminosity-redshift relation for the eFEDS hard X-ray sample compared to the *Swift*-BAT sample (Ricci et al. 2017) and approximate flux limit for the HEAO-1 A2 all-sky survey (Piccinotti et al. 1982). The eFEDS luminosities are absorption-corrected and dervied from the spectra (see Section 4.1). eFEDS probes a similar redshift range to *Swift*-BAT but samples luminosities around an order of magnitude fainter.

means it is much more complete in terms of obscured AGN, but Fig. 13 shows that the eFEDS hard sample, and by extension the eRASS, clearly probes to significantly fainter fluxes, as it is a true imaging survey, and hence luminosities are an order of magnitude lower at any given redshift. A combination of these surveys will undoubtedly yield new insights into the nature of the AGN population at low redshift.

Overall the eFEDS survey illustrates the high potential for the full eROSITA all-sky survey for studies of AGN physics and evolution, with the all-sky survey yielding unprecedented samples of hard X-ray AGN. A first taste of this has been presented in Waddell et al. (2024), who have presented the hard-selected sample from the first eROSITA sky survey eRASS1 (Merloni et al. 2024). Based on eFEDS, and applying approximate corrections for the sky area and the slightly deeper exposure compared to the expectation for the eRASS:8 survey, we would expected approximately 50 000 hard X-ray-selected AGN all-sky. While these will be mostly unobscured, the eFEDS analysis shows that objects with absorbing columns up to $N_H \sim 10^{24}$ cm^{-2} are sampled in the survey, so provided obscuration bias can be accurately characterised via the selection function, the eRASS has the potential to add significantly to AGN demographic studies. The information content of the resulting dataset will be very substantial, given the excellent eROSITA spectral response, especially when augmented by massive optical ground-based spectroscopy from SDSS and, eventually, 4MOST (de Jong et al. 2019; Merloni et al. 2019), both of which have dedicated eROSITA follow-up programs.

Data availability

The catalog is available at the CDS via anonymous ftp to `cdsarc.cds.unistra.fr` (`130.79.128.5`) or via `https://cdsarc.cds.unistra.fr/viz-bin/cat/J/A+A/693/A212`

Acknowledgements. FEB acknowledges support from ANID-Chile BASAL CATA FB210003, FONDECYT Regular 1200495, and Millennium Science Initiative Program – ICN12_009. RJA was supported by FONDECYT grant number 123171 and by the ANID BASAL project FB210003. MB, AG and BM are supported by the European Union's Innovative Training Network (ITN) 'BiD4BEST', funded by the Marie Sklodowska-Curie Actions in Horizon 2020 (GA N. 860744). MK acknowledges support from DLR grant FKZ 50 OR 2307. This work is based on data from eROSITA, the soft X-ray instrument aboard SRG, a joint Russian-German science mission supported by the Russian Space Agency (Roskosmos), in the interests of the Russian Academy of Sciences represented by its Space Research Institute (IKI), and the Deutsches Zentrum für Luft- und Raumfahrt (DLR). The SRG spacecraft was built by Lavochkin Association (NPOL) and its subcontractors, and is operated by NPOL with support from the Max Planck Institute for Extraterrestrial Physics (MPE). The development and construction of the eROSITA X-ray instrument was led by MPE, with contributions from the Dr. Karl Remeis Observatory Bamberg & ECAP (FAU Erlangen-Nuernberg), the University of Hamburg Observatory, the Leibniz Institute for Astrophysics Potsdam (AIP), and the Institute for Astronomy and Astrophysics of the University of Tübingen, with the support of DLR and the Max Planck Society. The Argelander Institute for Astronomy of the University of Bonn and the Ludwig Maximilians Universität Munich also participated in the science preparation for eROSITA. The eROSITA data shown here were processed using the eSASS and NRTA software systems developed by the German eROSITA consortium. The Hyper Suprime-Cam (HSC) collaboration includes the astronomical communities of Japan and Taiwan, and Princeton University. The HSC instrumentation and software were developed by the National Astronomical Observatory of Japan(NAOJ), the Kavli Institute for the Physics and Mathematics of the Universe (Kavli IPMU), the University of Tokyo, the High Energy Accelerator Research Organization (KEK), the Academia Sinica Institute for Astronomy and Astrophysics in Taiwan (ASIAA), and Princeton University. Funding was contributed by the FIRST program from Japanese Cabinet Office, the Ministry of Education, Culture, Sports, Science and Technology (MEXT), the Japan Society for the Promotion of Science (JSPS), Japan Science and Technology Agency (JST),the Toray Science Foundation, NAOJ, Kavli IPMU, KEK,ASIAA, and Princeton University. Funding for the Sloan Digital Sky Survey IV has been provided by the Alfred P. Sloan Foundation, the U.S. Department of Energy Office of Science, and the Participating Institutions. SDSS acknowledges support and resources from the Center for High-Performance Computing at the University of Utah. The SDSS web site is `www.sdss.org`. Funding for the Sloan Digital Sky Survey V has been provided by the Alfred P. Sloan Foundation, the Heising-Simons Foundation, the National Science Foundation, and the Participating Institutions. SDSS acknowledges support and resources from the Center for High-Performance Computing at the University of Utah. SDSS is managed by the Astrophysical Research Consortium for the Participating Institutions of the SDSS Collaboration, including the Carnegie Institution for Science, Chilean National Time Allocation Committee (CNTAC) ratified researchers, the Gotham Participation Group, Harvard University, Heidelberg University, The Johns Hopkins University, L'Ecole polytechnique fédérale de Lausanne (EPFL), Leibniz-Institut für Astrophysik Potsdam (AIP), Max-Planck-Institut für Astronomie (MPIA Heidelberg), Max-Planck-Institut für Extraterrestrische Physik (MPE), Nanjing University, National Astronomical Observatories of China (NAOC), New Mexico State University, The Ohio State University, Pennsylvania State University, Smithsonian Astrophysical Observatory, Space Telescope Science Institute (STScI), the Stellar Astrophysics Participation Group, Universidad Nacional Autónoma de México, University of Arizona, University of Colorado Boulder, University of Illinois at Urbana-Champaign, University of Toronto, University of Utah, University of Virginia, Yale University, and Yunnan University.

References

Abdollahi, S., Acero, F., Ackermann, M., et al. 2020, ApJS, 247, 33
Abramowicz, M. A., Czerny, B., Lasota, J. P., & Szuszkiewicz, E. 1988, ApJ, 332, 646
Aihara, H., Arimoto, N., Armstrong, R., et al. 2018, PASJ, 70, S4
Aird, J., Coil, A. L., Moustakas, J., et al. 2012, ApJ, 746, 90
Aird, J., Coil, A. L., Georgakakis, A., et al. 2015, MNRAS, 451, 1892
Akiyama, M., Ueda, Y., Ohta, K., Takahashi, T., & Yamada, T. 2003, ApJS, 148, 275
Alexander, D. M., Stern, D., Del Moro, A., et al. 2013, ApJ, 773, 125
Alexandroff, R. M., Zakamska, N. L., Barth, A. J., et al. 2018, MNRAS, 479, 4936
Almeida, A., Anderson, S. F., Argudo-Fernández, M., et al. 2023, ApJS, 267, 44
Antonucci, R. R. J., & Miller, J. S. 1985, ApJ, 297, 621
Arcodia, R., Campana, S., Salvaterra, R., & Ghisellini, G. 2018, A&A, 616, A170
Assef, R. J., Stern, D., Kochanek, C. S., et al. 2013, ApJ, 772, 26

Assef, R. J., Brightman, M., Walton, D. J., et al. 2020, ApJ, 897, 112
Awaki, H., Koyama, K., Inoue, H., & Halpern, J. P. 1991, PASJ, 43, 195
Baldry, I. K., Liske, J., Brown, M. J. I., et al. 2018, MNRAS, 474, 3875
Baronchelli, L., Nandra, K., & Buchner, J. 2020, MNRAS, 498, 5284
Blanton, M. R., Bershady, M. A., Abolfathi, B., et al. 2017, AJ, 154, 28
Bongiorno, A., Schulze, A., Merloni, A., et al. 2016, A&A, 588, A78
Boroson, T. A., & Green, R. F. 1992, ApJS, 80, 109
Brunner, H., Liu, T., Lamer, G., et al. 2022, A&A, 661, A1
Brusa, M., Comastri, A., Mignoli, M., et al. 2003, A&A, 409, 65
Brusa, M., Zamorani, G., Comastri, A., et al. 2007, ApJS, 172, 353
Brusa, M., Urrutia, T., Toba, Y., et al. 2022, A&A, 661, A9
Buchner, J. 2016, Statist. Comput., 26, 383
Buchner, J. 2019, PASP, 131, 108005
Buchner, J. 2021, J. Open Source Softw., 6, 3001
Buchner, J., & Bauer, F. E. 2017, MNRAS, 465, 4348
Buchner, J., Georgakakis, A., Nandra, K., et al. 2014, A&A, 564, A125
Buchner, J., Georgakakis, A., Nandra, K., et al. 2015, ApJ, 802, 89
Buchner, J., Schulze, S., & Bauer, F. E. 2017, MNRAS, 464, 4545
Chang, Y. L., Arsioli, B., Giommi, P., Padovani, P., & Brandt, C. H. 2019, A&A, 632, A77
Civano, F., Marchesi, S., Comastri, A., et al. 2016, ApJ, 819, 62
Cocchia, F., Fiore, F., Vignali, C., et al. 2007, A&A, 466, 31
Comastri, A., Setti, G., Zamorani, G., & Hasinger, G. 1995, A&A, 296, 1
Comparat, J., Merloni, A., Dwelly, T., et al. 2020, A&A, 636, A97
D'Abrusco, R., Álvarez Crespo, N., Massaro, F., et al. 2019, ApJS, 242, 4
de Jong, R. S., Agertz, O., Berbel, A. A., et al. 2019, The Messenger, 175, 3
Della Ceca, R., Maccacaro, T., Caccianiga, A., et al. 2004, A&A, 428, 383
Della Ceca, R., Caccianiga, A., Severgnini, P., et al. 2008, A&A, 487, 119
Dey, A., Schlegel, D. J., Lang, D., et al. 2019, AJ, 157, 168
Dotan, C., & Shaviv, N. J. 2011, MNRAS, 413, 1623
Dwelly, T., Salvato, M., Merloni, A., et al. 2017, MNRAS, 469, 1065
Eckart, M. E., Stern, D., Helfand, D. J., et al. 2006, ApJS, 165, 19
Evans, I. N., Primini, F. A., Glotfelty, K. J., et al. 2010, ApJS, 189, 37
Fabian, A. C., Vasudevan, R. V., & Gandhi, P. 2008, MNRAS, 385, L43
Fiore, F., Giommi, P., Vignali, C., et al. 2001, MNRAS, 327, 771
Fiore, F., Brusa, M., Cocchia, F., et al. 2003, A&A, 409, 79
Freyberg, M., Perinati, E., Pacaud, F., et al. 2020, SPIE Conf. Ser., 11444, 114441O
Gallagher, S. C., Brandt, W. N., Chartas, G., et al. 2006, ApJ, 644, 709
Georgakakis, A., Aird, J., Schulze, A., et al. 2017, MNRAS, 471, 1976
Gibson, R. R., Jiang, L., Brandt, W. N., et al. 2009, ApJ, 692, 758
Gilli, R., Comastri, A., & Hasinger, G. 2007, A&A, 463, 79
Giommi, P., Brandt, C. H., Barres de Almeida, U., et al. 2019, A&A, 631, A116
Greene, J. E., & Ho, L. C. 2005, ApJ, 630, 122
Green, P. J., Silverman, J. D., Cameron, R. A., et al. 2004, ApJS, 150, 43
Gunn, J. E., Siegmund, W. A., Mannery, E. J., et al. 2006, AJ, 131, 2332
Guo, H., Shen, Y., & Wang, S. 2018, Astrophysics Source Code Library [`record ascl:1809.008`]
Halpern, J. P. 1984, ApJ, 281, 90
Hartigan, J. A., & Hartigan, P. M. 1985, Ann. Statist., 13, 70
Hasinger, G., Cappelluti, N., Brunner, H., et al. 2007, ApJS, 172, 29
HI4PI Collaboration (Ben Bekhti, N., et al.) 2016, A&A, 594, A116
Huchra, J. P., Macri, L. M., Masters, K. L., et al. 2012, ApJS, 199, 26
Ilbert, O., Arnouts, S., McCracken, H. J., et al. 2006, A&A, 457, 841
Itoh, R., Utsumi, Y., Inoue, Y., et al. 2020, ApJ, 901, 3
Jones, D. H., Read, M. A., Saunders, W., et al. 2009, MNRAS, 399, 683
Jones, M. L., Hickox, R. C., Black, C. S., et al. 2016, ApJ, 826, 12
Kaastra, J. S., Mewe, R., Liedahl, D. A., Komossa, S., & Brinkman, A. C. 2000, A&A, 354, L83
Kaspi, S., Smith, P. S., Netzer, H., et al. 2000, ApJ, 533, 631
Kaspi, S., Brandt, W. N., George, I. M., et al. 2002, ApJ, 574, 643
Kelly, B. C., & Shen, Y. 2013, ApJ, 764, 45
Kenter, A., Murray, S. S., Forman, W. R., et al. 2005, ApJS, 161, 9
Kollmeier, J. A., Zasowski, G., Rix, H.-W., et al. 2017, arXiv e-prints [arXiv:`1711.03234`]
Koss, M., Trakhtenbrot, B., Ricci, C., et al. 2017, ApJ, 850, 74
Koss, M. J., Ricci, C., Trakhtenbrot, B., et al. 2022a, ApJS, 261, 2
Koss, M. J., Trakhtenbrot, B., Ricci, C., et al. 2022b, ApJS, 261, 1
La Franca, F., Fiore, F., Vignali, C., et al. 2002, ApJ, 570, 100
La Franca, F., Fiore, F., Comastri, A., et al. 2005, ApJ, 635, 864
Lang, D. 2014, AJ, 147, 108
Liu, T., Merloni, A., Wang, J.-X., et al. 2018, MNRAS, 479, 5022
Liu, A., Bulbul, E., Ghirardini, V., et al. 2022a, A&A, 661, A2
Liu, T., Buchner, J., Nandra, K., et al. 2022b, A&A, 661, A5
Liu, T., Merloni, A., Comparat, J., et al. 2022c, A&A, 661, A27
Luo, B., Brandt, W. N., Xue, Y. Q., et al. 2017, ApJS, 228, 2
Maiolino, R., Marconi, A., Salvati, M., et al. 2001, A&A, 365, 28
Maiolino, R., Risaliti, G., Salvati, M., et al. 2010, A&A, 517, A47
Markowitz, A. G., Krumpe, M., & Nikutta, R. 2014, MNRAS, 439, 1403
Massaro, E., Maselli, A., Leto, C., et al. 2015, Ap&SS, 357, 75
Merloni, A., Predehl, P., Becker, W., et al. 2012, arXiv e-prints [arXiv:`1209.3114`]
Merloni, A., Bongiorno, A., Brusa, M., et al. 2014, MNRAS, 437, 3550
Merloni, A., Alexander, D. A., Banerji, M., et al. 2019, The Messenger, 175, 42
Merloni, A., Lamer, G., Liu, T., et al. 2024, A&A, 682, A34
Murray, S. S., Kenter, A., Forman, W. R., et al. 2005, ApJS, 161, 1
Nandra, K., Laird, E. S., Aird, J. A., et al. 2015, ApJS, 220, 10
Nenkova, M., Sirocky, M. M., Nikutta, R., Ivezić, Ž., & Elitzur, M. 2008, ApJ, 685, 160
Nishizawa, A. J., Hsieh, B.-C., Tanaka, M., & Takata, T. 2020, arXiv e-prints [arXiv:`2003.01511`]
Oh, K., Koss, M., Markwardt, C. B., et al. 2018, ApJS, 235, 4
Page, M. J., Mittaz, J. P. D., & Carrera, F. J. 2001, MNRAS, 325, 575
Page, M. J., Carrera, F. J., Stevens, J. A., Ebrero, J., & Blustin, A. J. 2011, MNRAS, 416, 2792
Pavlinsky, M., Tkachenko, A., Levin, V., et al. 2021, A&A, 650, A42
Piccinotti, G., Mushotzky, R. F., Boldt, E. A., et al. 1982, ApJ, 253, 485
Pierre, M., Pacaud, F., Adami, C., et al. 2016, A&A, 592, A1
Predehl, P., Andritschke, R., Arefiev, V., et al. 2021, A&A, 647, A1
Proga, D., Stone, J. M., & Kallman, T. R. 2000, ApJ, 543, 686
Ranalli, P., Comastri, A., Vignali, C., et al. 2013, A&A, 555, A42
Revnivtsev, M., Sazonov, S., Jahoda, K., & Gilfanov, M. 2004, A&A, 418, 927
Ricci, C., Trakhtenbrot, B., Koss, M. J., et al. 2017, ApJS, 233, 17
Richards, G. T., Lacy, M., Storrie-Lombardi, L. J., et al. 2006, ApJS, 166, 470
Rothschild, R., Boldt, E., Holt, S., et al. 1979, Space Sci. Instrum., 4, 269
Salvato, M., Buchner, J., Budavári, T., et al. 2018, MNRAS, 473, 4937
Salvato, M., Wolf, J., Dwelly, T., et al. 2022, A&A, 661, A3
Salviander, S., Shields, G. A., Gebhardt, K., & Bonning, E. W. 2007, ApJ, 662, 131
Saxton, R. D., Read, A. M., Esquej, P., et al. 2008, A&A, 480, 611
Sazonov, S. Y., & Revnivtsev, M. G. 2004, A&A, 423, 469
Schlegel, D. J., Finkbeiner, D. P., & Davis, M. 1998, ApJ, 500, 525
Schneider, P. C., Freund, S., Czesla, S., et al. 2022, A&A, 661, A6
Schulze, A., Bongiorno, A., Gavignaud, I., et al. 2015, MNRAS, 447, 2085
Shen, Y. 2013, Bull. Astron. Soc. India, 41, 61
Shen, Y., & Liu, X. 2012, ApJ, 753, 125
Simmonds, C., Buchner, J., Salvato, M., Hsu, L. T., & Bauer, F. E. 2018, A&A, 618, A66
Smee, S. A., Gunn, J. E., Uomoto, A., et al. 2013, AJ, 146, 32
Smith, R. K., Brickhouse, N. S., Liedahl, D. A., & Raymond, J. C. 2001, ApJ, 556, L91
Suh, H., Civano, F., Trakhtenbrot, B., et al. 2020, ApJ, 889, 32
Sunyaev, R., Arefiev, V., Babyshkin, V., et al. 2021, A&A, 656, A132
Sutherland, W., & Saunders, W. 1992, MNRAS, 259, 413
Truemper, J. 1982, Adv. Space Res., 2, 241
Trump, J. R., Sun, M., Zeimann, G. R., et al. 2015, ApJ, 811, 26
Tsuzuki, Y., Kawara, K., Yoshii, Y., et al. 2006, ApJ, 650, 57
Turner, T. J., George, I. M., Nandra, K., & Mushotzky, R. F. 1997, ApJS, 113, 23
Ueda, Y., Takahashi, T., Inoue, H., et al. 1999, ApJ, 518, 656
Ueda, Y., Akiyama, M., Ohta, K., & Miyaji, T. 2003, ApJ, 598, 886
Ueda, Y., Akiyama, M., Hasinger, G., Miyaji, T., & Watson, M. G. 2014, ApJ, 786, 104
Vestergaard, M., & Peterson, B. M. 2006, ApJ, 641, 689
Vestergaard, M., & Wilkes, B. J. 2001, ApJS, 134, 1
Vulic, N., Hornschemeier, A. E., Haberl, F., et al. 2022, A&A, 661, A16
Waddell, S. G. H., Nandra, K., Buchner, J., et al. 2024, A&A, 690, A132
Webb, N. A., Coriat, M., Traulsen, I., et al. 2020, A&A, 641, A136
Wenger, M., Ochsenbein, F., Egret, D., et al. 2000, A&AS, 143, 9
Willingale, R., Starling, R. L. C., Beardmore, A. P., Tanvir, N. R., & O'Brien, P. T. 2013, MNRAS, 431, 394
Wright, E. L., Eisenhardt, P. R. M., Mainzer, A. K., et al. 2010, AJ, 140, 1868
Wu, Q., & Shen, Y. 2022, ApJS, 263, 42
Yaqoob, T., Warwick, R. S., & Pounds, K. A. 1989, MNRAS, 236, 153
Yip, C. W., Connolly, A. J., Vanden Berk, D. E., et al. 2004, AJ, 128, 2603

Appendix A: The eFEDS hard source catalogue

Table A.1. Columns in the catalogue

Column name	Description
	X-ray source properties from Brunner et al. (2022)
NAME	Source name
ID_SRC	Source ID in the eFEDS hard X-ray catalogue
ID_main	ID of the corresponding source in the eFEDS main X-ray catalogue
RA_CORR	X-ray right ascension (deg; J2000), astrometrically corrected
DEC_CORR	X-ray declination (deg; J2000), astrometrically corrected
RADEC_ERROR_CORR	combined positional uncertainty (arcsec)
DET_LIKE_band	source detection likelihood in band band; band 1,2,3 for 0.2–0.6, 0.6–2.3, and 2.3–5 keV, band 0 for combined 3-band likelihood
inArea90	Whether located inside the inner 90% area region of eFEDS
ML_RATE_band	source count rate (cts/s) in band 1,2,3,u,b1,b2,b3,b4
ML_CTS_band	source net counts in band 1,2,3,u,b1,b2,b3,b4
ML_FLUX_band	source flux (erg cm^{-2} s^{-1}) in band 1,2,3,u,b1,b2,b3,b4
	Multiband properties, mainly from Salvato et al. (2022)
CTP_quality	Counterpart quality
CTP_CLASS	Classification of the optical counterpart . For AGN it can be 2: ‘likely extraGalactic’ or 3: ‘secure extraGalactic’.
Redshift	redshift
RedshiftOrig	origin of redshift
RedshiftGrade	Redshift Grade . Grade 4 indicates high-quality photo-z. The highest value 5 indicates spec-z.
CTP_LS8_UNIQUE_OBJID	ID of the best LS8 counterpart
CTP_LS8_RA	Right ascension (deg; J2000) of the best LS8 counterpart
CTP_LS8_DEC	Declination (deg; J2000) of the best LS8 counterpart
W1	LS8 Wise W1 magnitude (AB)
W1_ERR	LS8 Wise W1 magnitude error
W2	LS8 Wise W2 magnitude (AB)
W2_ERR	LS8 Wise W2 magnitude error
LS8_g	LS8 g-band magnitude (AB)
LS8_g_ERR	LS8 g-band magnitude error
LS8_r	LS8 r-band magnitude (AB)
LS8_r_ERR	LS8 r-band magnitude error
LS8_z	LS8 z-band magnitude
LS8_z_ERR	LS8 z-band magnitude error
in_KiDS	Whether located inside the region of the KiDS survey
galNH	Total Galactic absorption column density (cm^{-2})
AGN	Boolean flag for the AGN subsample
	X-ray spectral properties
LxModel	Index of the selected model for X-ray luminosity measurement. 1: single-powerlaw; 3: powerlaw+blackbody; 4: powerlaw with Gamma fixed at 1.8. 0 means no luminosity measurement.
NHclass	Class of measurement of AGN N_H based on model 1, which can be 1: `uninformative`, 2: `unobscured`, 3: `mildly-measured`, and 4: `well-measured`.
Exposure	Exposure time from the X-ray spectral file (s)
SrcCts	Source net counts in the 0.2–5 keV band measured from the spectra
Rate_*band*	Net count rate in the 0.2–2.3, 0.2–0.5, 0.5–1, 1–2, 2–4.5, 2.3–5, and 5–8 keV bands (with *band* suffixes of d2_2d3, d2_d5, d5_1, 1_2, 2_4d5, 2d3_5, and 5_8) measured from the spectra
RateErr_*band*	Net count rate error in the corresponding energy band
BkgCts_*band*	Background counts in the 0.2–0.6, 0.6–2.3, 2.3–5, and 5–8 keV bands (with *band* suffixes of d2_d6, d6_2d3, 2d3_5, and 5_8)
BkgCtsErr_*band*	Background counts error in the corresponding energy band

Table A.1. Continued.

Column name	Description
FluxObsv_*suffix*_*band*_m*n*	Observed energy flux (erg cm^2 s^{-1}) in an observed-frame energy band *s* (0.5–2 keV) or *t* (2.3–5 keV); for all the models (m0–m5)
FluxCorr_*suffix*_*band*_m*n*	Absorption corrected energy flux (erg cm^2 s^{-1}) in an observed-frame energy band *s* (0.5–2 keV) or *t* (2.3–5 keV); for m1–m5
FluxIntr_*suffix*_*band*_m*n*	Absorption corrected energy flux (erg cm^2 s^{-1})) in a rest-frame energy band *s* (0.5–2 keV), *h* (2–10 keV), or *2keV* (1.999–2.001 keV); for m1–m5
LumiIntr_*suffix*_*band*_m*n*	Intrinsic (absorption corrected) luminosity (erg/s) in a rest-frame energy band *s* (0.5–2 keV), *h* (2–10 keV), or *2keV* (1.999–2.001 keV); for m1–m5. Having no model index suffix m*n* indicates the selected luminosity measurement using model LxModel.
logZ_m*n*	log Bayesian evidence for each mode (m0– m5)
Γ_*suffix*_m*n*	Powerlaw slope; for m1, m2, m3, m5
logPowNorm_*suffix*_m*n*	Power-law normalization for AGN models (m1∼m5)
lognH_*suffix*_m*n*	AGN absorption column density N_H (cm^{-2}) for AGN models, or Galactic N_H for m0
logBkgNorm_*suffix*_m*n*	Background normalization for all the models
logApecNorm_*suffix*	APEC normalization; only for m0
logBBNorm_*suffix*	Blackbody normalization; only for m3
logkT_*suffix*_m*n*	Temperature (keV) of blackbody (m3) or APEC (m0)
logAbundanc_*suffix*	Abundance of the APEC model; only for m0
dGm_*suffix*	Slope of the additional soft power law minus slope of the primary power law; only for m2
logFrac_*suffix*	Ratio of the additional power-law to the primary power law at 1 keV; only for m2
	SDSS optical spectral properties
SDSS_DR	SDSS data release version
PLATE	plate ID
MJD	MJD
FIBERID	Fiber ID
CATALOGID	catalogue ID
SDSS_RA	SDSS target RA [deg]
SDSS_DEC	SDSS target DEC [deg]
SDSS_Z	SDSS redshift
SNR_conti	continum signal-to-noise ratio
LogL1350	1350Åluminosity [erg/s]
LogL1350_err	1350Åluminosity [erg/s]
LogL3000	3000Åluminosity [erg/s]
LogL3000_err	3000Åluminosity [erg/s]
LogL5100	5100Åluminosity [erg/s]
LogL5100_err	5100Åluminosity [erg/s]
logMbh_Hbeta	Hbeta black hole mass
logMbh_Hbeta_err	Hbeta black hole mass 1σ error
logMBH_MgII	MgII black hole mass
logMBH_MgII_err	MgII black hole mass 1σ error
logMBH_CIV	CIV black hole mass
logMBH_CIV_err	CIV black hole mass 1σ error
Ha_br_flux	Hα flux
Ha_br_flux_err	Hα flux uncertainty
Ha_br_LogL	Hα luminosity
Ha_br_LogL_err	Hα luminosity uncertainty
Ha_br_FWHM	Hα FWHM
Ha_br_FWHM_err	Hα FWHM uncertainty
Hb_br_flux	Hβ flux
Hb_br_flux_err	Hβ flux uncertainty

Table A.1. Continued.

Column name	Description
Hb_br_LogL	Hβ luminosity
Hb_br_LogL_err	Hβ luminosity uncertainty
Hb_br_FWHM	Hβ FWHM
Hb_br_FWHM_err	Hβ FWHM uncertainty
MgII_br_flux	MgII flux
MgII_br_flux_err	MgII flux uncertainty
MgII_br_LogL	MgII luminosity
MgII_br_LogL_err	MgII luminosity uncertainty
MgII_br_FWHM	MgII FWHM
MgII_br_FWHM_err	MgII FWHM uncertainty
CIV_br_flux	CIV flux
CIV_br_flux_err	CIV flux uncertainty
CIV_br_LogL	CIV luminosity
CIV_br_LogL_err	CIV luminosity uncertainty
CIV_br_FWHM	CIV FWHM
CIV_br_FWHM_err	CIV FWHM uncertainty
Lbol	bolometric luminosity
Lbol_err	bolometric luminosity error
logMBH	adopted black hole mass
logMBH_err	adopted black hole mass error
Ledd	Eddington luminosity
Ledd_err	Eddington luminosity error
GoodMBH	whether the black hole mass is good

Notes. In the column names, the band flags indicate a few energy bands as listed in Table. A.2. The *suffix* flags in the flux-related columns (FluxObsv, FluxCorr, FluxIntr, LumiIntr) include 'Med' (posterior median), 'Lo1', 'Lo2' ($1\sigma/2\sigma$ percentile lower limit), 'Up1', 'Up2' ($1\sigma/2\sigma$ percentile upper limit), and 'BF' (best-fit). For other X-ray spectral parameters, the *suffix* flags include 'Med' (posterior median), 'Mean' (posterior mean), 'Std' (standard deviation), 'Lo' (1σ lower limit), 'Up' (1σ upper limit). For a few spectral shape parameters, for example, Γ and N_H, we also provide 'HLo' (1σ HDI lower limit), 'HUp' (1σ HDI upper limit), and 'KL' (KL divergence). These X-ray spectral parameters are named and calculated in the same way as described in Liu et al. (2022b).

Table A.2. Dictionary of energy band suffixes in the column names

Band	Energy range
1	0.2–0.6 keV
2	0.6–2.3 keV
3	2.3–5 keV
s	0.5–2 keV
t	2.3–5 keV
u	5–8 keV
b1	0.2–0.5 keV
b2	0.5–1 keV
b3	1–2 keV
b4	2–4.5 keV
2keV	1.999–2.001 keV